Post Flight Estimation of Aerodynamic Angles
of a Launch Vehicle in Windy Conditions

Vincenzo D'Antuono*, Alessandro Zavoli[†], and Guido De Matteis[‡]
Sapienza University of Rome, Via Eudossiana 18, 00184, Rome, Italy

Renato Zanetti[§]
The University of Texas at Austin, 78712, Austin, Texas

Simone Pizzurro[¶] and Enrico Cavallini[‖]
Italian Space Agency, Rome, 00133, Italy

This paper presents a filtering technique based on a consider Extended Kalman filter for estimating the aerodynamic angles and the wind components for the atmospheric flight phase of a launch vehicle, using measurements provided by an Inertial Measurement Unit, a GPS sensor, and an Air Data System. An original filter formulation is presented, where the wind speed components are considered as filter states in place of the aerodynamics angles, which are found *a-posteriori*. Also, a first-order Gauss-Markov process is used to account for the elastic rotation at the gimbal, while a multiplicative error quaternion formulation is adopted to provide an accurate yet robust reconstruction of the LV attitude.

Simulation results are presented and discussed for the flight of a realistic model of the Ares-I LV. The methodology appears suitable for the estimation of the angle of attack, sideslip angle, and wind speed components, albeit with a high level of uncertainty in model parameters knowledge and wind data.

I. Introduction

In this paper, a filtering technique for post-flight analyses is proposed to estimate the aerodynamic angles and the wind components during the atmospheric flight of a launch vehicle (LV). The dynamics of LVs exhibit unique characteristics during the first stage of flight, including rapid variations in inertial and aerodynamic parameters and interactions between low and high-frequency modes due to the slender shape of the vehicle. Accurately modeling the vehicle is challenging due to safety and cost constraints that limit dedicated flight tests with specific maneuvers.

The scope of this study is to provide a tool that can contribute to various areas of research, such as uncertainty quantification in LV models, where uncertainties arise from measurement errors, environmental conditions, and modeling assumptions. Therefore, developing robust techniques to accurately estimate and propagate these uncertainties remains a significant challenge. To this aim, an accurate description of the nonlinear LV dynamics is crucial to thoroughly test estimation methodologies, as they often rely on simplified process models, which are typically assumed to ensure both reliability and simplicity. A reliable estimator of aerodynamic angles and wind velocity is also beneficial to enhance the accuracy of the current balloon-based wind data collection method before launch and, for instance, improve the accuracy of post-flight trajectory reconstruction activities.

Various methodologies are proposed in the literature to estimate aerodynamic angles and wind profiles for flight vehicles. Karlgaard *et al.* [1] combines flight data from weather balloons, meteorological sounding rockets, and onboard pressure sensors to reconstruct the atmospheric density and winds. Vitale *et al.* [2] estimates the wind profile during a flight test of a reusable reentry vehicle using Gauss-Markov models and an Unscented Kalman Filter. Dutta *et al.* [3]

---

*PhD student, Department of Mechanical and Aerospace Engineering, vincenzo.dantuono@uniroma1.it

[†]Assistant Professor, Department of Mechanical and Aerospace Engineering, alessandro.zavoli@uniroma1.it

[‡]Professor, Department of Mechanical and Aerospace Engineering, guido.dematteis@uniroma1.it

[§]Associate Professor, Department of Aerospace Engineering and Engineering Mechanics, renato@utexas.edu

[¶]Research Fellow, Space Transportation, Space Infrastructures, and In-Orbit Servicing Department, Via del Politecnico snc, Rome, 00133, Italy; simone.pizzurro@est.asi.it

[‖]Head of Space Transportation Programs Office, Space Transportation, Space Infrastructures, and In-Orbit Servicing Department, Via del Politecnico snc, Rome, 00133, Italy; enrico.cavallini@asi.it

evaluates trajectory, angles of attack, sideslip, and atmospheric parameters for a Mars planetary entry mission using sensor measurements and filtering techniques.

Other studies solve the same estimation problem in real-time, with the aim of improving the management of structural loads for LVs in load-alleviation systems. The use of wind sensors, either true or virtual, as well as a LIDAR wind sensor, is proposed by Boelitz *et al.*[4] in order to provide near real-time wind measurements. In Ref. [5], the aerodynamic angles are determined for load-relief feedback by a Kalman filter that accounts for a simplified LV dynamical model and uses measurements of lateral accelerations provided by the inertial navigation system (INS). Within the same application area, Simplicio *et al.*[6, 7] present a disturbance observer for onboard wind anticipation that drives a load-relief compensator.

An estimator based on a *consider* version of the Extended Kalman filter (CEKF) [8] is proposed in this study where the components of the wind speed are considered as filter states and the aerodynamics angles are determined *a-posteriori*. Unlike a previous work by the same authors [9], the method propagates the airspeed velocity components and uses the true airspeed as measurement. A multiplicative error quaternion formulation (MEKF) is also adopted. The process model takes into account the elastic rotation of the section perpendicular to the nozzle null rotation axis at the gimbal location so as to estimate the effect of elasticity on the thrust direction. The effects of non-collocated sensors are also accounted for in terms of their displacement from c.g. location, with the goal of improving model fidelity.

The paper is organized as follows. The mathematical model of the vehicle is first recalled, with reference to a medium-fidelity simulation model of the Ares-I LV in atmospheric flight. Next, the principal aspects and mathematical framework of sequential filtering are recalled, and the state and measurement equations for the CMEKF are reported. Results obtained by simulations and Monte Carlo campaigns are then presented and discussed with the objective of evaluating the performance and suitability of the approach. A section of conclusions ends the paper.

II. Mathematical Model

A. Launch vehicle

The LV model features a 6 degree-of-freedom rigid-body dynamics, a spherical Earth with constant angular rate $\omega_\oplus$, and static aerodynamic and thrust forces and moments. Inertial coupling due to nozzle rotation is taken into consideration, and Thrust Vector Control (TVC) actuator dynamics is modeled by a second-order transfer function with a pure delay to represent hardware processing time, where gimbal angles and angular rates have saturation limits. Finally, the structural dynamics of the model are represented by the first three bending modes, while sloshing and aeroelastic effects are neglected. Reference is made to Appendix .A.6 for the definition of the reference frames.

Specific symbols and notation are employed in what follows. In particular, he angular rate of frame $\mathcal{F}_A$ relative to $\mathcal{F}_C$ is represented by the vector ω_{AC}. When a vector is denoted with a subscript $[A]$, it is expressed in the frame $\mathcal{F}_A$. If not explicitly mentioned, vectors are assumed to be represented in the body frame $\mathcal{F}_B$. The rotation matrix from frame $\mathcal{F}_A$ to $\mathcal{F}_C$ is indicated as $\mathcal{R}_{CA}$.

The equations of motion for the LV are expressed in $\mathcal{F}_B$ as

$$m\left(\dot{v} + \omega_{BI} \times v + \mathcal{R}_{BF}\omega_\oplus \times v + \mathcal{R}_{BF}\left(\omega_\oplus \times \omega_\oplus \times p_{[F]}\right)\right) = F_g + T + F_A + F_N \tag{1}$$

$$I\dot{\omega}_{BI} + \omega_{BI} \times (I\omega_{BI}) = M_A + M_T + M_N \tag{2}$$

where the Earth angular rate $\omega_\oplus = [0, 0, \omega_\oplus]^T$, with $\omega_\oplus = 7.291\,985 \times 10^{-5}\,\text{rad/s}$, represents the velocity of frame $\mathcal{F}_F$ relative to $\mathcal{F}_I$, and v and p are the ground speed and inertial position of the vehicle c.g., respectively. Assuming a simple inverse square model for the gravity field, the weight force is given by

$$\mathbf{F}_g = \mathcal{R}_{BE} \begin{bmatrix} 0 \\ 0 \\ g \end{bmatrix} \tag{3}$$

where the rotation matrix $\mathcal{R}_{BE}$ is expressed using the Shuster's quaternion multiplication [10] as follows

$$\mathcal{R}_{BE} = I - 2e_0[e_\times] + 2[e_\times]^2 \tag{4}$$

being e_0 and e, respectively, the scalar and vector part of the quaternion $\bar{e} = [e_0, e]$, I the identity matrix, and $[e_\times]$ the skew-symmetric matrix formed from the vector part of quaternion e.

A TVC is used to orient the thrust direction for control and stabilization purposes. The thrust force $\mathbf{T}$ is applied at the nozzle pivot point and directed along the x-axis of a frame $\mathcal{F}_N$ fixed to the nozzle. The nozzle orientation with respect to the LV airframe $\mathcal{F}_B$ is given by the matrix $\mathcal{R}_{NB} = R_2(\delta_z)R_3(\delta_y)$ that reads

$$\mathcal{R}_{NB} = \begin{bmatrix} \cos(\delta_z) & 0 & \sin(\delta_z) \\ 0 & 1 & 0 \\ -\sin(\delta_z) & 0 & \cos(\delta_z) \end{bmatrix} \begin{bmatrix} \cos(\delta_y) & -\sin(\delta_y) & 0 \\ \sin(\delta_y) & \cos(\delta_y) & 0 \\ 0 & 0 & 1 \end{bmatrix} \tag{5}$$

being δ_y and δ_z the nozzle rotation angles (also referred for the sake of simplicity as the TVC angles).

As a result of the nozzle rotation commanded by the TVC, the components of the thrust vector in the body frame are expressed as

$$\mathbf{T} = \mathbf{T}_{rig} + \begin{bmatrix} 0 \\ T_{rig\,y}\sigma_{Gy} \\ T_{rig\,z}\sigma_{Gz} \end{bmatrix}, \tag{6}$$

where T is the thrust magnitude, $\mathbf{T}_{rig}$ is the ideal thrust not considering the elastic deformation of the vehicle, given by

$$\mathbf{T}_{rig} = \begin{bmatrix} T_{rig\,x} \\ T_{rig\,y} \\ T_{rig\,z} \end{bmatrix} = \mathcal{R}_{NB}^T \begin{bmatrix} T \\ 0 \\ 0 \end{bmatrix}, \tag{7}$$

and the rotation matrix $\mathcal{R}_{NB}$ is given by Eq.(5). The angles σ_{Gy} and σ_{Gz} represent the (additional) gimbal rotations with respect to the undeformed axis due to the flexible degrees of freedom. Note that σ_{Gx} is zero as the elastic deformation in the axial direction is neglected. The moment due to the thrust is expressed as

$$\mathbf{M}_T = (l_g + \boldsymbol{\phi}_G) \times \mathbf{T} \tag{8}$$

where $l_g = [l_{g_x}, l_{g_y}, l_{g_z}]^T$ is the position vector of the nozzle pivot point.

The quasi-steady-state aerodynamic force and moment read

$$\mathbf{F}_A = \begin{bmatrix} -D \\ C \\ -N \end{bmatrix}, \qquad \mathbf{M}_A = l_{ap} \times \begin{bmatrix} -D \\ C \\ -N \end{bmatrix} + \begin{bmatrix} QSb\left[C_{l_\alpha}(M)\alpha + C_{l_\beta}(M)\beta\right] \\ QSbC_{m_\alpha}(M)\alpha \\ QSbC_{n_\beta}(M)\beta \end{bmatrix} \tag{9}$$

where $l_{ap} = [l_{xap}, l_{yap}, l_{zap}]^T$ is the position vector of the aerodynamic reference point (AP), and D, C, and N are the axial (drag), lateral, and normal force components, respectively, given by

$$\begin{aligned} D &= QSC_A(M) - F_{\text{base}} \\ C &= QSC_{Y\beta}(M)\beta \\ N &= QSC_{N\alpha}(M)\alpha \end{aligned} \tag{10}$$

where $C_A(M)$ is the axial-force coefficient, $C_{Y_\beta}(M)$ and $C_{N_\alpha}(M)$ are the slopes of the side-force and normal force coefficients with respect to β and α, respectively, expressed in tabular form as functions of the Mach number (M). The aerodynamic derivatives $C_{l_\alpha}(M)$, $C_{l_\beta}(M)$, $C_{m_\alpha}(M)$, and $C_{n_\beta}(M)$ also depend on M. In Eqs. 10 $Q = \frac{1}{2}\rho V_a^2$ is the dynamic pressure, ρ is the atmospheric density, V_a is the airspeed modulus, b and S are the LV diameter and cross-section, respectively, and F_{base} is the base force term resulting from the aerodynamic interaction between the LV base and the surrounding fluid and/or exhaust flow, which depends on altitude.

The aerodynamic angles are

$$\alpha = \arctan\left(\frac{w_a}{u_a}\right) \tag{11}$$

$$\beta = \arctan\left(\frac{v_a}{\sqrt{u_a^2 + w_a^2}}\right) \tag{12}$$

and the airspeed is $\mathbf{V}_a = \mathbf{v} - \mathbf{v}_w$, where $\mathbf{v}$ and $\mathbf{v}_w$ are the ground and wind speeds, respectively, is written as

$$\mathbf{V}_a = \begin{bmatrix} u_a \\ v_a \\ w_a \end{bmatrix} = V_a \begin{bmatrix} \cos\alpha\cos\beta \\ \sin\beta \\ \sin\alpha\cos\beta \end{bmatrix} \tag{13}$$

The actuator dynamics is described by a cascade of two transfer functions, that model a second-order system and a pure delay $\tau = 20$ ms due to the hardware processing time, that is approximated by a second-order Padè approximation, according to

$$\begin{bmatrix} \dot{d} \\ \ddot{d} \end{bmatrix} = \begin{bmatrix} 0 & 1 \\ -\frac{12}{\tau^2} & -\frac{6}{\tau} \end{bmatrix} \begin{bmatrix} d \\ \dot{d} \end{bmatrix} + \begin{bmatrix} 0 \\ -\frac{12}{\tau^2} \end{bmatrix} \delta_c \tag{14}$$

$$\delta_{\tilde{c}} = \dot{d} + \delta_c \tag{15}$$

where δ_c is the TVC command, and $\delta_{\tilde{c}}$ is the delayed version of the same signal, given by $\delta_{\tilde{c}} = \dot{d} + \delta_c$. The transfer function of the TVC dynamics is

$$W_{TVC}(s) = \frac{\delta}{\delta_{\tilde{c}}} = \frac{\omega_{TVC}^2}{s^2 + 2\zeta_{TVC}\omega_{TVC}s + \omega_{TVC}^2} \tag{16}$$

where ζ_{TVC} and ω_{TVC} represent the damping ratio and natural frequency, respectively.

To account for the vehicle elasticity, the first three lateral bending modes are considered while neglecting the coupling between pitch and yaw lateral modes due to the axial symmetry of the vehicle[11]. The model reads

$$\ddot{\mathbf{q}} + 2\zeta\mathbf{\Omega}\dot{\mathbf{q}} + \mathbf{\Omega}^2\mathbf{q} = \bar{\mathbf{\Phi}}_G\mathbf{T} \tag{17}$$

where ζ is the damping ratio, set to 0.005 [12], $\mathbf{\Omega}$ is the natural frequency matrix, and $\bar{\mathbf{\Phi}}_G$ is the mass-normalized displacement matrix at the pivot point. The vector $\mathbf{q}$ indicates the generalized coordinates, and the relation $\boldsymbol{\phi}_G = \bar{\mathbf{\Phi}}_G\mathbf{q}$ holds, where $\boldsymbol{\phi}_G$ represents the physical displacements at the nozzle pivot point G. Similarly, using the mode slope matrix $\bar{\mathbf{\Sigma}} = \frac{d}{d\mathbf{q}}\bar{\mathbf{\Phi}}$, the angular displacement (σ_G), rate ($\dot{\sigma}_G$), and acceleration ($\ddot{\sigma}_G$) at the same point are computed. As for the elastic motion of the structure at IMU location, it results in $\boldsymbol{\phi}_{IMU} = \bar{\mathbf{\Phi}}\mathbf{q}$, $\dot{\boldsymbol{\phi}}_{IMU} = \bar{\mathbf{\Phi}}\dot{\mathbf{q}}$, and $\ddot{\boldsymbol{\phi}}_{IMU} = \bar{\mathbf{\Phi}}\ddot{\mathbf{q}}$ for linear displacement, velocity, and acceleration, respectively, where $\bar{\mathbf{\Phi}}$ is the displacement matrix at the sensor location. The angular displacement (σ_{IMU}), rate ($\dot{\sigma}_{IMU}$), and acceleration ($\ddot{\sigma}_{IMU}$) at the same IMU location are also computed.

The effects of nozzle rotation in terms of force and moment in $\mathcal{F}_b$ are [12]

$$\mathbf{F}_N = m_N\boldsymbol{l}_n \times \dot{\boldsymbol{\omega}}_N + \boldsymbol{\omega}_{BI} \times (m_N\boldsymbol{l}_n \times \boldsymbol{\omega}_N) \tag{18}$$

$$\mathbf{M}_N = (\boldsymbol{I}_N - \boldsymbol{l}_g \times m_N\boldsymbol{l}_n\times)\dot{\boldsymbol{\omega}}_N + \boldsymbol{\omega}_{BI} \times (\boldsymbol{I}_N - \boldsymbol{l}_g \times m_N\boldsymbol{l}_n\times)\boldsymbol{\omega}_N \tag{19}$$

Given the nozzle mass m_N, and the position vectors $\boldsymbol{l}_g$ and $\boldsymbol{l}_n$ in $\mathcal{F}_b$, where $\boldsymbol{l}_n$ is the distance between nozzle pivot point and nozzle c.g., it is

$$\boldsymbol{l}_g = \begin{bmatrix} -x_g \\ 0 \\ 0 \end{bmatrix} \qquad \boldsymbol{l}_n = \begin{bmatrix} -x_n\cos(\beta_\psi)\cos(\beta_\theta) \\ -x_n\sin(\beta_\psi) \\ x_n\sin(\beta_\theta)\cos(\beta_\psi) \end{bmatrix} \tag{20}$$

and, the nozzle angular rate $\boldsymbol{\omega}_N$ and its derivative $\dot{\boldsymbol{\omega}}_N$, respectively

$$\boldsymbol{\omega}_N = \begin{bmatrix} \sin(\beta_\theta)\dot{\beta}_\psi \\ \dot{\beta}_\theta \\ \cos(\beta_\theta)\dot{\beta}_\psi \end{bmatrix} \tag{21}$$

$$\dot{\boldsymbol{\omega}}_N = \begin{bmatrix} \sin(\beta_\theta)\ddot{\beta}_\psi + \cos(\beta_\theta)\dot{\beta}_\psi\dot{\beta}_\theta \\ \ddot{\beta}_\theta \\ -\sin(\beta_\theta)\dot{\beta}_\psi\dot{\beta}_\theta + \cos(\beta_\theta)\ddot{\beta}_\psi \end{bmatrix} \tag{22}$$

Assuming a diagonal inertia matrix of the nozzle $I_N = \mathcal{R}_{BN} I_{N[N]} \mathcal{R}_{NB} \approx I_{N[N]}$, valid in the case of small rotations between the frames $\mathcal{F}_b$ and $\mathcal{F}_N$, that is

$$I_N = \begin{bmatrix} I_{N_x} & 0 & 0 \\ 0 & I_{N_y} & 0 \\ 0 & 0 & I_{N_z} \end{bmatrix} \tag{23}$$

the components of $\mathbf{F}_N$ and $\mathbf{M}_N$ are expressed as

$$
\begin{aligned}
F_{N_x} = m_N x_n \Big[& \left(\sin(\beta_\theta) \dot{\beta}_\psi \dot{\beta}_\theta - \cos(\beta_\theta) \ddot{\beta}_\psi \right) \sin(\beta_\psi) \\
& + q \sin(\beta_\psi) \sin(\beta_\theta) \dot{\beta}_\psi - q \cos(\beta_\psi) \cos(\beta_\theta) \dot{\beta}_\theta \\
& - r \cos(\beta_\psi) \dot{\beta}_\psi - \sin(\beta_\theta) \cos(\beta_\psi) \ddot{\beta}_\theta \Big]
\end{aligned}
\tag{24}
$$

$$
\begin{aligned}
F_{N_y} = m_N x_n \Big[& - \left(\sin(\beta_\psi) \sin(\beta_\theta) \dot{\beta}_\psi - \cos(\beta_\psi) \cos(\beta_\theta) \dot{\beta}_\theta \right) p \\
& - \left(\sin(\beta_\psi) \cos(\beta_\theta) \dot{\beta}_\psi + \sin(\beta_\theta) \cos(\beta_\psi) \dot{\beta}_\theta \right) r + \cos(\beta_\psi) \ddot{\beta}_\psi \Big]
\end{aligned}
\tag{25}
$$

$$
\begin{aligned}
F_{N_z} = m_N x_n \Big[& \left(\sin(\beta_\theta) \ddot{\beta}_\psi + \cos(\beta_\theta) \dot{\beta}_\psi \dot{\beta}_\theta \right) \sin(\beta_\psi) + p \cos(\beta_\psi) \dot{\beta}_\psi \\
& + q \sin(\beta_\psi) \cos(\beta_\theta) \dot{\beta}_\psi + q \sin(\beta_\theta) \cos(\beta_\psi) \dot{\beta}_\theta - \cos(\beta_\psi) \cos(\beta_\theta) \ddot{\beta}_\theta \Big]
\end{aligned}
\tag{26}
$$

$$
\begin{aligned}
M_{N_x} = & - I_{N_x} \left(\sin(\beta_\theta) \ddot{\beta}_\psi + \cos(\beta_\theta) \dot{\beta}_\psi \dot{\beta}_\theta \right) \\
& + \left[I_{N_y} \dot{\beta}_\theta - m_N x_n x_g \left(\sin(\beta_\psi) \sin(\beta_\theta) \dot{\beta}_\psi - \cos(\beta_\psi) \cos(\beta_\theta) \dot{\beta}_\theta \right) \right] r \\
& - \left(I_{N_z} \cos(\beta_\theta) + m_N x_n x_g \cos(\beta_\psi) \right) q \dot{\beta}_\psi
\end{aligned}
\tag{27}
$$

$$
\begin{aligned}
M_{N_y} = & - I_{N_x} r \sin(\beta_\theta) \dot{\beta}_\psi - I_{N_y} \ddot{\beta}_\theta + m_N x_n x_g \Big[\left(\sin(\beta_\theta) \ddot{\beta}_\psi + \cos(\beta_\theta) \dot{\beta}_\psi \dot{\beta}_\theta \right) \sin(\beta_\psi) \\
& - \cos(\beta_\psi) \cos(\beta_\theta) \ddot{\beta}_\theta \Big] + \left(I_{N_z} \cos(\beta_\theta) + m_N x_n x_g \cos(\beta_\psi) \right) p \dot{\beta}_\psi
\end{aligned}
\tag{28}
$$

$$
\begin{aligned}
M_{N_z} = & I_{N_x} q \sin(\beta_\theta) \dot{\beta}_\psi + I_{N_z} \left(\sin(\beta_\theta) \dot{\beta}_\psi \dot{\beta}_\theta - \cos(\beta_\theta) \ddot{\beta}_\psi \right) \\
& - m_N x_n x_g \cos(\beta_\psi) \ddot{\beta}_\psi - \left[I_{N_y} \dot{\beta}_\theta - m_N x_n x_g \left(\sin(\beta_\psi) \sin(\beta_\theta) \dot{\beta}_\psi - \cos(\beta_\psi) \cos(\beta_\theta) \dot{\beta}_\theta \right) \right] p
\end{aligned}
\tag{29}
$$

where β_θ and β_ψ are the angles between the $\mathcal{F}_B$ and $\mathcal{F}_N$ x-axis and y-axis, respectively, and p, q, and r are the components of ω_{BI} components.

B. Sensor models

Measurements from various sensors, including IMU, GNSS receiver, and an ADS, are used for estimation purposes. The IMU, usually placed ahead of the c.g., provides measurements of the inertial non-gravitational acceleration $\mathbf{a}_{\text{IMU}}$ and the body-to-inertial angular rate ω_{BI} in the frame $\mathcal{F}_B$. The IMU location for the considered application is reported in Table 1, where the coordinates are expressed in the structural reference frame $\mathcal{F}_S$ (see Appendix .A.6). Systematic errors and noise that affect the measurements are modeled according to Ref. [13]. Consequently, the accelerometer and gyro data are modeled as follows

$$\tilde{a}_{\text{IMU}} = (I + \Lambda_a + M_a + N_a) a_{\text{IMU}} + \beta_a + w_a \tag{30}$$

$$\dot{\beta}_a = w_{b_a} \tag{31}$$

$$\tilde{\omega}_{BI} = (I + \Lambda_\omega + M_\omega + N_\omega) \omega_{BI} + \beta_\omega + w_g \tag{32}$$

$$\dot{\beta}_\omega = w_{b_g} \tag{33}$$

Measured quantities are denoted by a tilde, w is a zero mean white Gaussian noise, while the subscripts a and g indicate accelerometer and gyro, respectively. Matrices $\Lambda_i = \text{diag}(\lambda_i)$, $M_i = [\mu_i \times]$, and $N_i = N(\nu_i)$, denote scale

factor, misalignment, and non-orthogonality, respectively. The notation $[\boldsymbol{\mu}_i \times]$ refers to the skew-matrix form of vector $\boldsymbol{\mu}_i$ for cross product, and $\boldsymbol{N}$ is given by

$$
\boldsymbol{N}(\boldsymbol{v}) = \begin{bmatrix} 0 & v_z & v_y \\ v_z & 0 & v_x \\ v_y & v_x & 0 \end{bmatrix} \tag{34}
$$

An ideal ADS sensor is considered, as uncertainties in Mach number and total air temperature, which contribute to the definition of the measurement error model in the ADS system, are ignored for the sake of simplicity [**?**]. Therefore, it is assumed that the sensor gives the TAS measurement, as

$$
\tilde{V}_{\mathrm{T}} = \sqrt{u_a^2 + v_a^2 + w_a^2} + w_{V_{\mathrm{T}}} \tag{35}
$$

subjected to random noise $w_{V_{\mathrm{T}}}$ white and Gaussian in nature. Correction factors used to compensate for effects related to the location of the sensor [14] are not considered for the sake of simplicity.

The GNSS receiver, whose location is reported in Table 1, provides position and velocity output in the $\mathcal{F}_F$ frame. The position output is expressed as

$$
\tilde{\boldsymbol{r}}_{\mathrm{GNSS}_{[F]}} = \boldsymbol{r}_{\mathrm{GNSS}_{[F]}} + \boldsymbol{w}_{r,c} + \boldsymbol{w}_{r,w} \tag{36}
$$

$$
\dot{\boldsymbol{w}}_{r,c} = -\frac{1}{\tau_c} \boldsymbol{w}_{r,c} + \boldsymbol{w}_{d,w} \tag{37}
$$

where $\boldsymbol{r}_{\mathrm{GNSS}_{[F]}}$ and $\tilde{\boldsymbol{r}}_{\mathrm{GNSS}_{[F]}}$ are, the true and measured positions of the receiver in the ECEF reference frame, $\mathcal{F}_F$, respectively. The simplified model used to describe the position error incorporates a combination of an uncorrelated (white) random noise and a correlated noise sequence, represented by a first-order Markov process. The velocity measurement is expressed as

$$
\tilde{\boldsymbol{v}}_{\mathrm{GNSS}_{[F]}} = \boldsymbol{v}_{\mathrm{GNSS}_{[F]}} + \boldsymbol{w}_v \tag{38}
$$

where $\boldsymbol{v}_{\mathrm{GNSS}_{[F]}}$ and $\tilde{\boldsymbol{v}}_{\mathrm{GNSS}_{[F]}}$ are the true and measured planet-relative velocity vectors, respectively, with components again specified in $\mathcal{F}_F$, and $\boldsymbol{w}_v$ is a white and Gaussian noise.

Reference is to be made to [15] for further details on the sensor models.

III. Estimation Methodology

The present paper adopts a novel formulation of the filter, where the components of the wind speed are used as filter states instead of the aerodynamic angles, which, in turn, are calculated after the filtering process. A MEKF is adopted [8] for attitude estimation where, neglecting higher-order terms, the four-component quaternion can be effectively replaced by a three-component error vector. This approach is highly effective when dealing with small attitude errors.

The process equations feature first-order Markov processes for the wind velocity. The elastic rotations in the pitch and yaw planes at the nozzle gimbal are also described using the same processes. In facts, the LV angular rate components oscillate at a relatively low frequency (below 1 Hz) due to the forcing action of the transversal thrust components generated by the TVC, which is then projected onto the dynamics of the first elastic mode (with a natural frequency of 1 Hz) (see Eq.(17)). Consequently, the gimbal point oscillates at the same frequency, causing variations of the thrust axis direction that require correction. Finally, random walk processes are introduced to capture and compensate for accelerometer and gyro biases, and scale factors, whereas the effects of misalignment and non-orthogonality errors are neglected in the filter.

The state vector $\boldsymbol{x}$ of the filter is

$$
\boldsymbol{x}(t) = \left[u_a, v_a, w_a, u_{w_{[E]}}, v_{w_{[E]}}, w_{w_{[E]}}, \delta_{\sigma_y}, \delta_{\sigma_z}, e_0, e_1, e_2, e_3, r, \phi, \theta, \boldsymbol{\beta}_a, \boldsymbol{\beta}_\omega, \boldsymbol{\lambda}_a, \boldsymbol{\lambda}_\omega \right]^T \tag{39}
$$

where $[u_a, v_a, w_a]$ are the airspeed components in $\mathcal{F}_B$, $[u_w, v_w, w_w]_{[E]}$ are the wind components in $\mathcal{F}_E$, $\delta_{\sigma_y}, \delta_{\sigma_z}$ are the elastic pitch and yaw angular displacements at the gimbal location, respectively, and $[e_0, e_1, e_2, e_3,]$ are the attitude quaternion. The position vector of the c.g. of the LV is expressed in terms of geocentric radius r, latitude ϕ, and longitude θ. Next, the vectors $\boldsymbol{\beta}_a = [\beta_{a,x}, \beta_{a,y}, \beta_{a,z}]^T$, $\boldsymbol{\lambda}_a = [\lambda_{a,x}, \lambda_{a,y}, \lambda_{a,z}]^T$, $\boldsymbol{\beta}_\omega = [\beta_{\omega,x}, \beta_{\omega,y}, \beta_{\omega,z}]^T$, and $\boldsymbol{\lambda}_\omega = [\lambda_{\omega,x}, \lambda_{\omega,y}, \lambda_{\omega,z}]^T$ are, respectively, accelerometer biases and scale factors, and gyro biases and scale factors.

Table 1   Parameters of sensor error models.

Sensor	Parameter	Name	Value	Unit	Location in $\mathcal{F}_S$ [m]
IMU	σ_{w_a}	noise, velocity random walk	[100 100 100]	$\mu g/\sqrt{Hz}$	
	σ_{w_ω}	noise, angle random walk	[0.005 0.005 0.005]	$deg/\sqrt{h}$	
	$\sigma_{w_{b_a}}$	bias stability	$[1.38\ 1.38\ 1.38]\cdot 10^{-5}$	$\mu g/\sqrt{h}$	
	$\boldsymbol{\beta}_a\|_{t=0}$	bias constant, accelerometer	[100 100 100]	μg	
	$\sigma_{w_{b_\omega}}$	bias rate, random walk	$[6.94\ 6.94\ 6.94]\cdot 10^{-9}$	$deg/h^{3/2}$	[45 -0.14 1.52]
	$\boldsymbol{\beta}_\omega\|_{t=0}$	bias constant, gyro	[0.02 0.02 0.02]	deg/h	
	λ_a	scale factor, accelerometer	[50 50 50]	ppm	
	λ_ω	scale factor, gyro	[30 30 30]	ppm	
	$\boldsymbol{\mu}_a$	misalignment, accelerometer	[60 60 60]	μrad	
	$\boldsymbol{\mu}_\omega$	misalignment, gyro	[60 60 60]	μrad	
	$\boldsymbol{\nu}_a$	non-orthogonality, accelerometer	[30 30 30]	μrad	
	$\boldsymbol{\nu}_\omega$	non-orthogonality, gyro	[30 30 30]	μrad	
GNSS	τ_c	autocorrelation time	1800	s	
	$\sigma_{w_{d,w}}$	driving noise on position	1	m/s	
	$\sigma_{w_{r,w}}$	noise on position	6	m	[62.91 1.05 -0.92]
	σ_{w_v}	noise on velocity	1	m/s	
ADS	σ_{w_T}	noise on TAS	5	m/s	/
Nozzle angles	σ_{w_δ}	noise on nozzle angle	0.1	deg	/

The input vector $\boldsymbol{u}$ is

$$\boldsymbol{u}(t) = \left[\tilde{\delta}_y^{cmd}, \tilde{\delta}_z^{cmd}, p, q, r, a_x\right]^T$$

where p, q, r and a_x have the known meaning, and $\tilde{\delta}_y^{cmd} = \delta_y^{cmd} + w_\delta$ and $\tilde{\delta}_z^{cmd} = \delta_z^{cmd} + w_\delta$ are the TVC command angles in the pitch and yaw planes, respectively, affected by the noise $w_\delta \sim \mathcal{N}(0, \sigma_{w_\delta}^2)$. The values of σ_{w_δ} are reported in Tab. 1, As usual, the notation $\mathcal{N}(0, \boldsymbol{Q})$ indicates a zero-mean white Gaussian noise characterized by the variance matrix $\boldsymbol{Q}$.

A. Process model

1. IMU systematic errors

The true angular rates, denoted as $\boldsymbol{\omega}_{BI} = [p, q, r]$ are defined in terms of the measured angular rates $\tilde{\boldsymbol{\omega}}_{BI}$ provided by the rate gyros of the IMU, and can be expressed as follows

$$\boldsymbol{\omega}_{BI} = (\boldsymbol{I} + \boldsymbol{\Lambda}_\omega)^{-1}(\tilde{\boldsymbol{\omega}}_{BI} - \boldsymbol{\beta}_\omega) \tag{40}$$

and a_x the longitudinal component of the acceleration in $\mathcal{F}_B$ at c.g. location modeled as follow

$$\boldsymbol{a} = (\boldsymbol{I} + \boldsymbol{\Lambda}_a)^{-1}(\tilde{\boldsymbol{a}}_{IMU} - \boldsymbol{\beta}_a) - (\boldsymbol{\omega}_{BI} \times (\boldsymbol{\omega}_{BI} \times \boldsymbol{d}_{IMU}) - \dot{\boldsymbol{\omega}}_{BI} \times \boldsymbol{d}_{IMU} \tag{41}$$

where measured acceleration and angular rate are modeled as $\tilde{\boldsymbol{a}}_{IMU} = \boldsymbol{a}_{IMU} + \boldsymbol{\eta}_a$ and $\tilde{\boldsymbol{\omega}}_{BI} = \boldsymbol{\omega}_{BI} + \boldsymbol{\eta}_\omega$ with $\boldsymbol{\eta}_\omega \sim \mathcal{N}(0, \sigma_{w_\omega}^2)$ and $\boldsymbol{\eta}_a \sim \mathcal{N}(0, \sigma_{w_a}^2)$. The vector $\boldsymbol{d}_{IMU}$ denotes the position vector of the IMU sensor in reference frame $\mathcal{F}_B$, and $\dot{\boldsymbol{\omega}}_{BI}$ represents a smoothed finite-difference estimate of the actual angular acceleration expressed as

$$\dot{\boldsymbol{\omega}}_{BI} = (\boldsymbol{I} + \boldsymbol{\Lambda}_\omega)^{-1}(\dot{\tilde{\boldsymbol{\omega}}}_{BI} - \boldsymbol{\beta}_\omega) \tag{42}$$

which is derived from the measured angular velocity $\tilde{\omega}_{BI}$. Accelerometer, gyro bias and scale factors $\boldsymbol{\beta}_a, \boldsymbol{\beta}_\omega, \boldsymbol{\lambda}_a, \boldsymbol{\lambda}_\omega$ respectively, are modeled as a zero-order Markov process

$$\dot{\boldsymbol{\beta}}_a = \boldsymbol{\eta}_{\beta_a} \tag{43}$$

$$\dot{\boldsymbol{\beta}}_\omega = \boldsymbol{\eta}_{\beta_\omega} \tag{44}$$

$$\dot{\boldsymbol{\lambda}}_a = \boldsymbol{\eta}_{\lambda_a} \tag{45}$$

$$\dot{\boldsymbol{\lambda}}_\omega = \boldsymbol{\eta}_{\lambda_\omega} \tag{46}$$

where $\boldsymbol{\eta}_{\beta_a} \sim \mathcal{N}(0, \boldsymbol{Q}_{\beta_a})$, $\boldsymbol{\eta}_{\beta_\omega} \sim \mathcal{N}(0, \boldsymbol{Q}_{\beta_\omega})$, $\boldsymbol{\eta}_{\lambda_a} \sim \mathcal{N}(0, \boldsymbol{Q}_{\lambda_a})$, $\boldsymbol{\eta}_{\lambda_\omega} \sim \mathcal{N}(0, \boldsymbol{Q}_{\lambda_\omega})$.

2. Airspeed

In the filter process equations, the variations of the airspeed components are expressed as

$$\dot{u}_a = a_x - (w_a + w_w)(q - \eta_{\omega_y} + q_\oplus) + (v_a + v_w)(r - \eta_{\omega_z} + r_\oplus) - \dot{u}_w + \varpi_x + f_{g_x} \tag{47}$$

$$\dot{v}_a = a_y + (w_a + w_w)(p - \eta_{\omega_x} + p_\oplus) - (u_a + u_w)(r - \eta_{\omega_z} + r_\oplus) - \dot{v}_w + \varpi_y + f_{g_y} \tag{48}$$

$$\dot{w}_a = a_z - (v_a + v_w)(p - \eta_{\omega_x} + p_\oplus) + (u_a + u_w)(q - \eta_{\omega_y} + q_\oplus) - \dot{w}_w + \varpi_z + f_{g_z} \tag{49}$$

where

$$a_y = \frac{1}{m}\left(\frac{1}{2}\rho V_T^2 S C_{Y_\beta} \arctan\left(\frac{v_a}{\sqrt{u_a^2 + w_a^2}}\right) - T\sin(\tilde{\delta}_z^{cmd} + \delta_{\sigma_z} + \eta_{\delta_z})\cos(\tilde{\delta}_y^{cmd} + \delta_{\sigma_y} + \eta_{\delta_y})\right) \tag{50}$$

$$a_z = \frac{1}{m}\left(-\frac{1}{2}\rho V_T^2 S C_{N_\alpha} \arctan\left(\frac{w_a}{u_a}\right) + T\sin(\tilde{\delta}_y^{cmd} + \delta_{\sigma_y} + \eta_{\delta_y})\right) \tag{51}$$

and $f_{g_x}, f_{g_y}, f_{g_z}$ are the components of the gravity acceleration in $\mathcal{F}_B$. Further details on the derivation of Eqs. (47)–(49) can be found in Appendix .A.6.

3. Relative position

The kinematic equations for LV position are written as follows

$$\begin{bmatrix} \dot{r} \\ \dot{\theta} \\ \dot{\phi} \end{bmatrix} = \begin{bmatrix} 0 & 0 & -1 \\ 0 & \frac{1}{r\cos\phi} & 0 \\ \frac{1}{r} & 0 & 0 \end{bmatrix} \left(\mathcal{R}_{EB} \begin{bmatrix} u_a \\ v_a \\ w_a \end{bmatrix} + \begin{bmatrix} u_w \\ v_w \\ w_w \end{bmatrix}_{[E]} \right) \tag{52}$$

$$\tag{53}$$

4. Attitude

The kinematics of quaternions is represented as follows

$$\begin{bmatrix} \dot{e}_0 \\ \dot{\boldsymbol{e}} \end{bmatrix} = \frac{1}{2}\left(\begin{bmatrix} -\boldsymbol{e}^T \\ e_0\boldsymbol{I} + [\boldsymbol{e}\times] \end{bmatrix}\right)\boldsymbol{\omega}_{BE} \tag{54}$$

the equation in question represents the variation of the rigid body's attitude concerning the reference frame $\mathcal{F}_E$, where

$$\boldsymbol{\omega}_{BE} = \boldsymbol{\omega}_{BI} - \mathcal{R}_{BE}\boldsymbol{\omega}_{EI} \tag{55}$$

being $\boldsymbol{\omega}_{EI}$ the NED-to-ECI angular velocity in $\mathcal{F}_E$

$$\boldsymbol{\omega}_{EI} = [(\dot{\theta} + \omega_\oplus)\cos\phi, \ -\dot{\phi}, \ -(\dot{\theta} + \omega_\oplus)\sin\phi]^T \tag{56}$$

Since the MEKF approach involves a multiplicative error formulation (in place of the classical additive formulation), a quaternion error vector δq is introduced as

$$\delta q = \hat{q}^{-1} \otimes q \tag{57}$$

where the symbol ˆ refers to the estimated quantity and $q = [e_0 \quad e]^T$ and the operator $\otimes$ is the Hamilton quaternion product.

The equations of attitude kinematics are

$$\begin{bmatrix} \dot{\hat{e}}_0 \\ \dot{\hat{e}} \end{bmatrix} = \frac{1}{2} \underbrace{\begin{bmatrix} 0 & -\hat{\omega}_{BE}^T \\ \hat{\omega}_{BE} & -[\hat{\omega}_{BE}\times] \end{bmatrix}}_{\Omega(\hat{\omega})} \begin{bmatrix} \hat{e}_0 \\ \hat{e} \end{bmatrix} \tag{58}$$

and, in compact form

$$\dot{\hat{q}} = \frac{1}{2} \begin{bmatrix} 0 \\ \hat{\omega}_{BE} \end{bmatrix} \otimes \hat{q} \tag{59}$$

Accordingly, the quaternion error dynamics reads [8]

$$\delta\dot{q} = -\begin{bmatrix} 0 \\ [\hat{\omega}_{BE}\times]e \end{bmatrix} + \frac{1}{2}\delta q \otimes \begin{bmatrix} 0 \\ \delta\omega_{BE} \end{bmatrix} \tag{60}$$

the first-order approximation of which is

$$\delta\dot{q} = -\begin{bmatrix} 0 \\ [\hat{\omega}_{BE}\times]e \end{bmatrix} + \frac{1}{2}\begin{bmatrix} 0 \\ \delta\omega_{BE} \end{bmatrix} \tag{61}$$

In order to obtain the process equation for the attitude error, the error dynamics is rewritten in terms of $\delta\alpha = 2\delta e$, as

$$\delta\dot{e}_0 = 0 \tag{62}$$
$$\delta\dot{\alpha} = -[\hat{\omega}_{BE}\times]\delta\alpha + \delta\omega_{BE} \tag{63}$$

At this point, Eq. (55) is considered for the expression of the error on angular rate $\delta\omega_{BE} = \omega_{BE} - \hat{\omega}_{BE}$, where the matrix $\mathcal{R}_{BE}$ is associated with the one estimated through the attitude error, in the form

$$\mathcal{R}_{BE} = \mathcal{R}_{BE}(\delta q)\hat{\mathcal{R}}_{BE}(q) \tag{64}$$

When the Euler's angles are sufficiently small the first-order approximation of the rotation matrix can be used, that is, $\mathcal{R}_{BE}(\delta q) \approx I_{3x3} - [\delta\alpha\times]$ [8]. By substituting the approximation $(I_{3x3} + \Lambda_\omega)^{-1} \approx (I_{3x3} - \Lambda_\omega)$ into Eq. (40) and assuming that scale factors are small enough, Eq. (63) becomes

$$\delta\dot{\alpha} = [(I_{3x3} - \hat{\Lambda}_\omega)(\tilde{\omega}_{BI} - \hat{\beta}_\omega)\times]\delta\alpha - \left[\left(\underbrace{\begin{bmatrix} \tilde{\omega}_{BI,x} & 0 & 0 \\ 0 & \tilde{\omega}_{BI,y} & 0 \\ 0 & 0 & \tilde{\omega}_{BI,z} \end{bmatrix}}_{\tilde{\Omega}_g} - \underbrace{\begin{bmatrix} \hat{\beta}_{\omega,x} & 0 & 0 \\ 0 & \hat{\beta}_{\omega,y} & 0 \\ 0 & 0 & \hat{\beta}_{\omega,z} \end{bmatrix}}_{\hat{B}_g}\right)\left(\lambda_\omega - \hat{\lambda}_\omega\right) + \right.$$
$$\left. + (I_{3x3} - \hat{\Lambda}_\omega)(\beta_\omega - \hat{\beta}_\omega) + (I_{3x3} - \hat{\Lambda}_\omega)\eta_\omega \right] - \hat{\mathcal{R}}_{BE}(q)(\omega_{EI} - \hat{\omega}_{EI}) \tag{65}$$

5. Wind components

The time derivatives of wind velocity components are represented as first-order Markov processes where the steady-state wind profile is assumed known with W the mean and λ the wind direction. For the Down velocity component

of the wind, the mean is considered equal to zero. Accordingly,

$$
\begin{bmatrix} \dot{u}_w \\ \dot{v}_w \\ \dot{w}_w \end{bmatrix}_{[E]} = \begin{bmatrix} -\frac{1}{\tau_{wl}}(u_{w_{[E]}} + W\sin(\pi/2 + \lambda)\eta_W) + \eta_{u_w} \\ -\frac{1}{\tau_{wl}}(v_{w_{[E]}} + W\cos(\pi/2 + \lambda)\eta_W) + \eta_{v_w} \\ -\frac{1}{\tau_{wd}}(w_{w_{[E]}}) + \eta_{w_w} \end{bmatrix} \tag{66}
$$

with process noise that takes into account the uncertainty on the mean value of wind speed in the form $\eta_W \sim \mathcal{N}(0, Q_W)$, and the turbulence noise, namely, $\eta_{u_w} \sim \mathcal{N}(0, Q_{u_w})$, $\eta_{v_w} \sim \mathcal{N}(0, Q_{v_w})$ and $\eta_{w_w} \sim \mathcal{N}(0, Q_{w_w})$. In order to use the wind acceleration in Eqs. (47),(48) and (49), Eq.(66) is written in the $\mathcal{F}_B$ frame

$$
\begin{bmatrix} \dot{u}_w \\ \dot{v}_w \\ \dot{w}_w \end{bmatrix} = \mathcal{R}_{BE} \begin{bmatrix} \dot{u}_w \\ \dot{v}_w \\ \dot{w}_w \end{bmatrix}_{[E]} + \omega_{BE} \times \mathcal{R}_{BE} \begin{bmatrix} u_w \\ v_w \\ w_w \end{bmatrix}_{[E]} \tag{67}
$$

The constant values of correlation times τ_{wl} and τ_{wd} are obtained using an autocorrelation of the lateral (north and east) and Down components of the wind velocity respectively. Figure 1 shows an example of the normalized autocorrelation
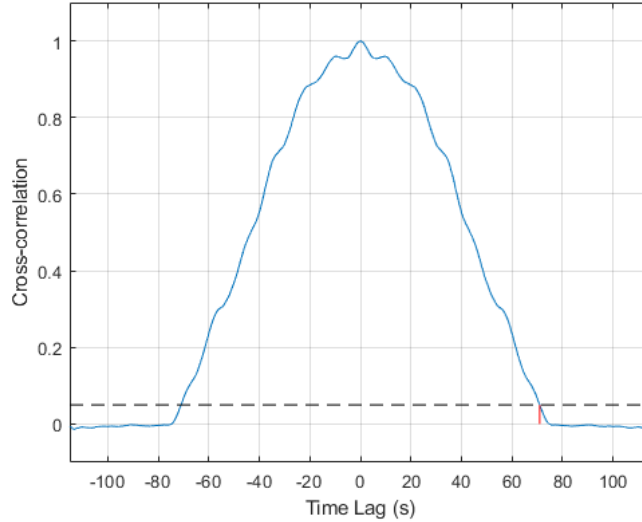

Fig. 1   **Normalized autocorrelation function of the North component of the wind velocity** $u_{w_{[E]}}$.

function of the North component of wind speed. The correlation time is obtained as one-third of the time shift (marked in the figure by a red bar line) where the function value is 0.05 [16]. This gives the same value, $\tau_{wl} = 71/3$ s, for the lateral components, and $\tau_{wd} = 28/3$ s for the downward component.

6. Elastic displacement

The last process equations deal with the angular displacements, due to the elastic degrees of freedom at the gimbal point, which are modeled as first-order Markov processes, that is

$$
\dot{\delta}_{\sigma_y} = -\frac{1}{\tau_{\sigma_y}}\delta_{\sigma_y} + \eta_{\delta_{\sigma_y}} \tag{68}
$$

$$
\dot{\delta}_{\sigma_z} = -\frac{1}{\tau_{\sigma_z}}\delta_{\sigma_z} + \eta_{\delta_{\sigma_z}} \tag{69}
$$

The correlation times $\tau_{\sigma_y} = \tau_{\sigma_z} = 5/3$ s have been specified by a trial and error procedure, while $\eta_{\delta_{\sigma_y}} \sim \mathcal{N}(0, Q_{\delta_{\sigma_y}})$ $\eta_{\delta_{\sigma_z}} \sim \mathcal{N}(0, Q_{\delta_{\sigma_z}})$.

Summing up, the process noise vector $\boldsymbol{\eta} \in \mathcal{R}^{23}$ is

$$\boldsymbol{\eta} = \left[\eta_{a,x}, \boldsymbol{\eta}_\omega, \eta_\delta, \eta_W, \eta_{u_w}, \eta_{v_w}, \eta_{w_w}, \eta_{\delta_{\sigma_y}}, \eta_{\delta_{\sigma_y}}, \boldsymbol{\eta}_{\beta_a}, \boldsymbol{\eta}_{\beta_\omega}, \boldsymbol{\eta}_{\lambda_a}, \boldsymbol{\eta}_{\lambda_\omega} \right] \tag{70}$$

B. Measurement model

Turning to the measurement model of the filter, the acceleration $\tilde{\boldsymbol{a}}_{\text{IMU}}$ provided by IMU is written as

$$\boldsymbol{a}_{\text{IMU}} = \boldsymbol{a} + \left(\boldsymbol{\omega}_{BI} \times (\boldsymbol{\omega}_{BI} \times \boldsymbol{d}_{\text{IMU}}) + \dot{\boldsymbol{\omega}}_{BI} \times \boldsymbol{d}_{\text{IMU}} + 2\boldsymbol{\omega}_{BI} \times \dot{\boldsymbol{d}}_{\text{IMU}} + \ddot{\boldsymbol{d}}_{\text{IMU}} \right) + \boldsymbol{\xi}_a \tag{71}$$

where only the y and z components are employed as measurements, and $\boldsymbol{\xi}_a \sim \mathcal{N}(0, \sigma_{w_a}^2)$. Next, $\boldsymbol{d}_{\text{IMU}}$ represents the position vector of the IMU in $\mathcal{F}_B$, while the terms $\dot{\boldsymbol{d}}_{\text{IMU}}$ and $\ddot{\boldsymbol{d}}_{\text{IMU}}$ are related to the sensor-shift in position due to c.g. variation in time and the elastic degrees of freedom.

$$a_y = \frac{1}{m} \left(\frac{1}{2}(P_1 + \xi_{P_1})V_T^2 \arctan\left(\frac{v_a}{\sqrt{u_a^2 + w_a^2}} \right) - T\sin(\tilde{\delta}_z^{cmd} + \delta_{\sigma_z} + \xi_\delta)\cos(\tilde{\delta}_y^{cmd} + \delta_{\sigma_y} + \xi_\delta) \right) \tag{72}$$

$$a_z = \frac{1}{m} \left(-\frac{1}{2}(P_2 + \xi_{P_2})V_T^2 \arctan\left(\frac{w_a}{u_a} \right) + T\sin(\tilde{\delta}_y^{cmd} + \delta_{\sigma_y} + \xi_\delta) \right) \tag{73}$$

The same model given by Eqs. (50)-(51) has been adopted for the a_y and a_z components of the true acceleration $\boldsymbol{a}$ at c.g. location, where the measurement noise has been added as shown in Eq.(72) and Eq.(73), where, as for the process equations, the measurement noise on the nozzle commands ($\tilde{\delta}_y^{cmd}$ and $\tilde{\delta}_z^{cmd}$) is considered as $\xi_\delta \sim \mathcal{N}(0, \sigma_{w_\delta}^2)$. Also, a noise is associated with the uncertain parameters

$$P_1 = \rho S C_{Y_\beta} \qquad P_2 = \rho S C_{N_\alpha} \tag{74}$$

being $\xi_{P_1} \sim \mathcal{N}(0, \sigma_{P_1}^2)$, $\xi_{P_2} \sim \mathcal{N}(0, \sigma_{P_2}^2)$.

Note that in the present measurement model the terms $\dot{\boldsymbol{d}}_{\text{IMU}}$ and $\ddot{\boldsymbol{d}}_{\text{IMU}}$ terms are neglected in the measurement model, and the additive noises $\xi_{a,y} \sim \mathcal{N}(0, \sigma_{w_{a,y}}^2)$, $\xi_{a,z} \sim \mathcal{N}(0, \sigma_{w_{a,z}}^2)$ are used to take into consideration the effects of the (otherwise unmodeled) elastic dynamics.

The measurement equations of the GNSS sensor are written as follows

$$\boldsymbol{r}_{\text{GNSS}_{[F]}} = \boldsymbol{r}_{[F]} + \mathcal{R}_{FB}\,\boldsymbol{\delta}_{\text{GNSS}_{[B]}} + \boldsymbol{\xi}_r \tag{75}$$

$$\boldsymbol{v}_{\text{GNSS}_{[F]}} = \mathcal{R}_{FE}\left(\mathcal{R}_{EB}\boldsymbol{v}_a + \boldsymbol{v}_w + [\boldsymbol{\omega}_{\oplus[E]} \times]\mathcal{R}_{EF}\boldsymbol{r}_{[F]} \right) + \mathcal{R}_{FB}[\boldsymbol{\omega}_{BE} \times]\,\boldsymbol{\delta}_{\text{GNSS}_{[B]}} + \boldsymbol{\xi}_v$$

where $\boldsymbol{\xi}_r \sim \mathcal{N}(0, \boldsymbol{R}_r)$ and $\boldsymbol{\xi}_v \sim \mathcal{N}(0, \boldsymbol{R}_v)$ have the known meaning and $\boldsymbol{\delta}_{GNSS}$ is the receiver lever arm from the LV c.g.

The position vector of the LV center of gravity in the frame $\mathcal{F}_F$ is

$$\boldsymbol{r}_{[F]} = r[\cos\theta\cos\phi, \ \sin\theta\cos\phi, \ \sin\phi]^T \tag{76}$$

whereas $\boldsymbol{\omega}_{BE}$ is the vehicle angular rate with respect to the NED reference frame, with components in $\mathcal{F}_B$. $\boldsymbol{\omega}_{\oplus[E]} = \omega_\oplus[-\cos\theta\cos\phi, \ -\sin\theta, \ -\cos\phi\sin\phi]^T$ is the Earth angular rate in the $\mathcal{F}_E$ frame.

Note that $\mathcal{R}_{FB}$ is obtained as $(\mathcal{R}_{BE}\mathcal{R}_{EF})^T$, where $\mathcal{R}_{BE}$ is given by Eq. (4), and $\mathcal{R}_{EF}$ is a transformation matrix depending only on the LV latitude and longitude, given by

$$\mathcal{R}_{EF} = \begin{bmatrix} -\cos\theta\sin\phi & -\sin\theta\sin\phi & \cos\phi \\ -\sin\theta & \cos\theta & 0 \\ -\cos\theta\cos\phi & -\cos\phi\sin\theta & -\sin\phi \end{bmatrix} \tag{77}$$

The true airspeed measurement equation is

$$V_T = \sqrt{u_a^2 + v_a^2 + w_a^2} + \xi_{V_T} \tag{78}$$

where $\xi_{V_T} \sim \mathcal{N}(0, \sigma_{w_T}^2)$. In conclusion, the measurement vector $y \in \mathcal{R}^9$ and the measurement noise vector $\xi \in \mathcal{R}^{12}$ are as follows

$$y = \left[a_{\text{IMU},y}, a_{\text{IMU},z}, r_{GNSS}, v_{GNSS}, V_T \right] \tag{79}$$

$$\xi = \left[\xi_{a,y}, \xi_{a,z}, \xi_v, \xi_{V_T}, \xi_\delta, \xi_r, \xi_{P_1}, \xi_{P_2} \right] \tag{80}$$

C. Consider Multiplicative Extended Kalman Filter

The challenge in the estimation problem at hand for the nonlinear dynamical system described in III.A is represented by the high number of parameters, primarily linked to the IMU systematic error sources. Additionally, there is the estimation of the quaternions, which are not represented by vectors but rather by groups, while a Kalman filter is designed to estimate states represented by vectors. The solution implemented in the present work is a Consider Multiplicative Extended Kalman Filter (CMEKF) [17, 18]. The filter performs an iterative estimation of the state vector by merging information from sensor measurements, that is, IMU, GNSS, and ADS (for the TAS). To enhance accuracy, uncertain parameters in the model may be disregarded if their impact on the state propagation is minimal. Alternatively, for improved precision, uncertain parameters can be treated as unknown values and estimated alongside other states. However, the latter approach increases the state dimension and consequently the computational burden. The Consider version of the EKF offers a solution by explicitly addressing the uncertainty associated with certain model parameters without estimating their values. This leads to a state estimator that exhibits robustness concerning parametric model uncertainty while keeping the state dimension unchanged. The CMEKF formulation implies partitioning the state vector as

$$x = \left[x_c, p \right]^T \tag{81}$$

where

$$x_c = \left[u_a, v_a, w_a, u_w, v_w, w_w, \delta_{\sigma_y}, \delta_{\sigma_z}, e_0, e_1, e_2, e_3, r, \phi, \theta, \lambda_{a,x} \right] \tag{82}$$

and

$$p = \left[\beta_{a,x}, \beta_{a,y}, \beta_{a,z}, \beta_{\omega,x}, \beta_{\omega,y}, \beta_{\omega,z}, \lambda_{a,y}, \lambda_{a,z}, \lambda_{\omega,x}, \lambda_{\omega,y}, \lambda_{\omega,z} \right] \tag{83}$$

For a continuous-discrete EKF [8], with an initial state estimate $\hat{x}_{0|0}$ and initial state covariance matrix $P_{0|0}$, the *a priori* estimate of the system state at time t_k, $\hat{x}_{k|k-1}$ with covariance $P_{k|k-1}$, is determined by solving the Cauchy problem

$$\dot{\hat{x}} = \hat{f}(\hat{x}, u, \eta, t) \qquad\qquad \forall t \in [t_{k-1}, t_k] \tag{84}$$

$$\dot{P} = F(t)P(t) + P(t)F(t)^T + G(t)Q(t)G(t)^T \qquad\qquad \forall t \in [t_{k-1}, t_k] \tag{85}$$

$$\hat{x}(t_{k-1}) = \hat{x}_{k-1|k-1} \tag{86}$$

$$P(t_{k-1}) = P_{k-1|k-1} \tag{87}$$

where the matrices F and G are obtained differentiating the system $\dot{\hat{x}}_P = \hat{f}(\hat{x}_P, \hat{q}_{k|k-1}, u, \eta, t)$ w.r.t $\hat{x}_P$ and η respectively. The vector x_P is defined as

$$x_P = \left[u_a, v_a, w_a, u_w, v_w, w_w, \delta_{\sigma_y}, \delta_{\sigma_z}, \delta\alpha, r, \phi, \theta, \beta_a, \beta_\omega, \lambda_a, \lambda_\omega \right] \tag{88}$$

where the vector part of the attitude error quaternion $\delta\alpha$ replace q- Moreover, the matrix $\mathcal{R}_{BE}$ in $\hat{f}(\hat{x}_P, \hat{q}_{k|k-1}, u, \eta, t)$ is written as a function of $\delta\alpha$, $\mathcal{R}_{BE}(q_{k|k}) = (I_{3x3} - [\delta\alpha\times])\mathcal{R}_{BE}(\hat{q}_{k|k-1})$, and

$$\hat{f} = \hat{f}(\hat{x}_P, \hat{q}_{k|k-1}, u, \eta, t)\Big|_{\eta=0} \qquad F = \frac{\partial f}{\partial x_P}\Big|_{\hat{x}_{k|k-1}, \delta\alpha=0, u_k, \eta=0, t} \qquad G = \frac{\partial f}{\partial \eta}\Big|_{\hat{x}_{k|k-1}, \delta\alpha=0, u_k, \eta=0, t} \tag{89}$$

The *a posteriori* estimate of state $\hat{x}_{k|k}$ and covariance $P_{k|k}$, which accounts for the measures at time t_k, reads

$$\hat{x}_{k|k} = \hat{x}_{k|k-1} + K_k \underbrace{\left[y_k - h\left(\hat{x}_{P,k|k-1}, \hat{q}_{k|k-1}, u_k \right) \right]}_{\Delta y_k} \tag{90}$$

$$P_{k|k} = \left[I - K_k H_k(\hat{q}_{k|k-1}) \right] P_{k|k-1} \left[I - K_k H_k(\hat{q}_{k|k-1}) \right]^T + K_k D_k R_k D_k^T K_k^T \tag{91}$$

where Δy_k represents the measurement residual while the Eq.(91) is the Joseph form [19] of the error covariance update which helps maintain numerical stability in the presence of nonlinearities. The quaternion states are updated differently, as follows

$$\hat{q}_{k|k} = \hat{q}_{k|k-1} \otimes \frac{1}{2} \begin{bmatrix} 1 \\ \delta\hat{\alpha}_{k|k} \end{bmatrix} \tag{92}$$

and a normalization is then carried out in order to guarantee that $\hat{q}_{k|k}^T \hat{q}_{k|k} = 1$.

The Kalman gain K_k is defined as

$$K_k = P_{k|k-1} H_{k|k-1}(\hat{q}_{k|k-1})^T \underbrace{\left[H_{k|k-1}(\hat{q}_{k|k-1}) P_{k|k-1} H_{k|k-1}(\hat{q}_{k|k-1})^T + D_k R_k D_k^T \right]^{-1}}_{S} \tag{93}$$

where the rows corresponding to the CMEKF parameter vector p are set to zero so that $p_{k|k} = p_{k|k-1}$ [20]. The measurement vector y_k at time t_k is

$$y_k = h(\hat{x}_{P,k|k}, \hat{q}_{k|k}, u_k, \xi_k, k) \tag{94}$$

whereas S is the measurement residual covariance matrix and

$$H_k = \left. \frac{\partial h}{\partial x_P} \right|_{\hat{x}_{k|k-1}, \delta\alpha=0, u_k, \xi_k=0, t_k} \qquad D_k = \left. \frac{\partial h}{\partial \xi} \right|_{\hat{x}_{k|k-1}, \delta\alpha=0, u_k, \xi_k=0, t_k} \tag{95}$$

Finally, the aerodynamic angles are determined as functions of the estimated airspeed components, according to Eqs.(11)–(12). Their estimated covariance is computed using the relation $H_{V_a} P H_{V_a}^T$, where H_{V_a} represents the Jacobian of Eqs.(11) and (12) with respect to the estimated airspeed components, and P is the estimated error covariance matrix.

IV. Results and Discussion

This section presents the results obtained by considering the first-stage flight of the ARES-I LV, the model of which is reported in Ref. [11], from the Kennedy Space Center towards the International Space Station (ISS). Following the initial upward movement within the first 5 seconds of liftoff, there is a predetermined pitch-over rotation occurring between 5 and 10 seconds. This rotation initiates a Zero Lift Gravity Turn (ZLGT) maneuver lasting from 10 to 120 seconds. During this phase, the rocket utilizes gravity to adjust its velocity trajectory while simultaneously minimizing lateral aerodynamic forces. This is achieved by maintaining a low angle of attack and aligning the vehicle with the relative velocity vector. During this phase of flight, the LV reaches Mach 1 speed after 48 seconds. When the engines burn out, the LV is at an altitude of approximately 44 km with a velocity of about 1.2 km/s.

In the simulation, the primary maneuver of the LV is executed in the pitch plane, and the direction of the wind is 44 degrees from the North.
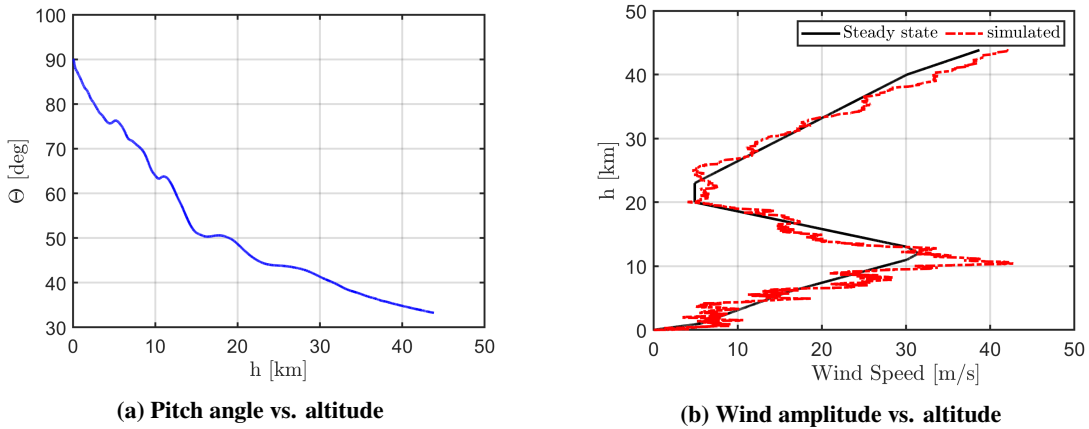

(a) Pitch angle vs. altitude

(b) Wind amplitude vs. altitude

Fig. 2   Vehicle pitch angle and wind profile for the simulated flight phase.

Figure 2 shows the pitch angle variation as a function of the altitude (Fig. 2a) and the specified wind profile (Fig. 2a). The latter is obtained by summing a three-dimensional stochastic wind vector, which passes a white noise signal through a Dryden filter, to a steady-state profile (black line) [21].
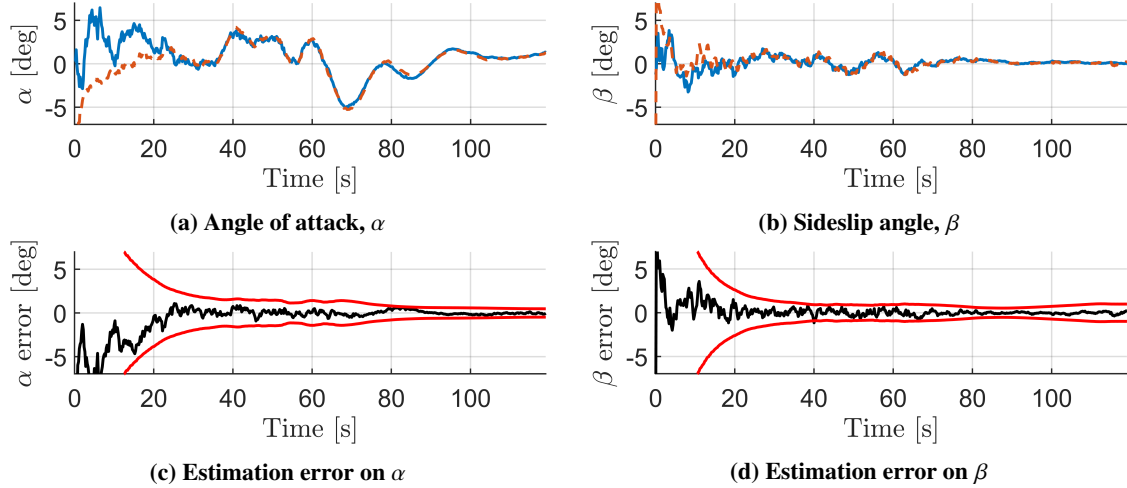
(a) Angle of attack, α

(b) Sideslip angle, β

(c) Estimation error on α

(d) Estimation error on β

Fig. 3   Results of the CMEKF filter for the aerodynamic angles: true (light blue), estimated (orange), 3-σ bounds (red), and estimation error (black).

Figure 3 reports the results of the estimation process and, in particular, the true and estimated values of the aerodynamic angles (light-blue and orange lines, respectively) are shown in Figs. 3a and 3b. Figures 3c and 3d complement this analysis by showing the estimation errors (black lines) and the 3-σ bounds (red lines), that are computed by taking the square root of the diagonal elements of the estimated covariance matrix.

(a) North wind, $u_{w[E]}$

(b) East wind, $v_{w[E]}$

(c) Down wind, $w_{w[E]}$

(d) Estimation error on $u_{w[E]}$

(e) Estimation error on $v_{w[E]}$
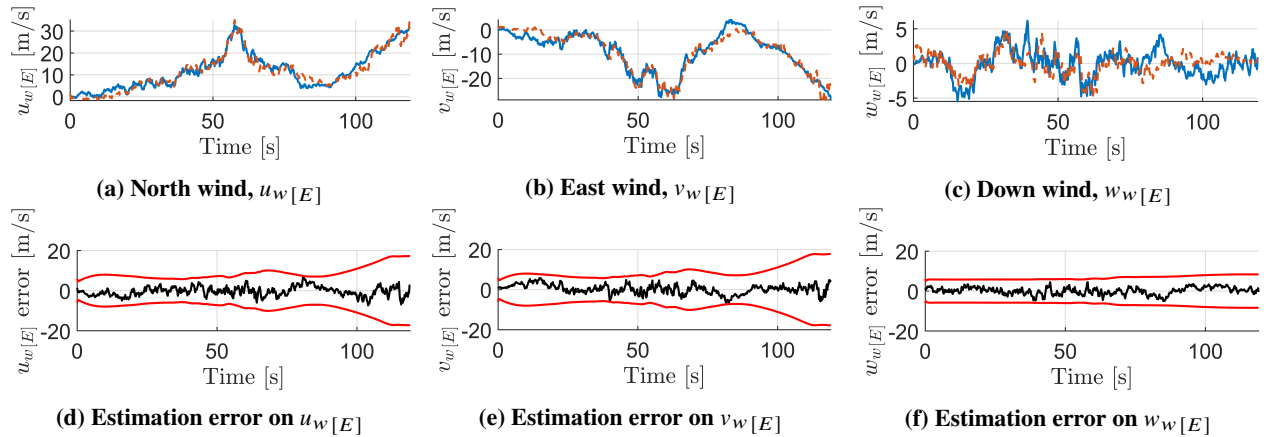
(f) Estimation error on $w_{w[E]}$

Fig. 4   Results of the CMEKF filter for the wind components: true value (light blue), estimated (orange), 3-σ bounds (red), and estimation error (black)

True and estimated variables, as well as estimation error and bounds, are shown in Fig. 4, for the North, East, and Down wind components. It is apparent that the filter is effective and provides adequate accuracy, most notably in the central portion of the flight. The accuracy of the aerodynamic angles estimation (Figs. 3a and 3b) is rather low in the first part of the simulation (about 12 s) when the LV velocity is low and significant variations of α and β are determined by relatively limited variations of wind speed. The estimation error also increases in the final part of the flight, particularly on the wind components (Figs. 4a and 4b) due, in this case, to the high speed of the vehicle (in comparison with wind speed) and the decreasing amplitude of aerodynamic actions being the air density very low at high altitude.

A. Monte Carlo analysis

The assessment of filter consistency and performance entails a comprehensive approach through Monte Carlo simulations. In these simulations, scattering uniformly distributed within specified ranges is introduced across model parameters, IMU systematic error sources, and wind and atmospheric characteristics. As for the scattering of model

parameters, specific attention is given to aerodynamic factors such as C_a, C_{N_α} and C_{Y_β}, that undergo variations of $\pm 10\%$ of their nominal values. Thrust is scattered through a range of $\pm 2\%$. As a consequence, the LM mass is scattered according to 2.

$$\dot{m} = -\frac{T}{g_0 ISP} \tag{96}$$

where g_0 denotes the acceleration due to gravity, and ISP represents the specific impulse. The time variations of thrust and mass are reported in Fig. 5b and Fig. 5c, where their nominal values (the data available for the filter) are depicted in black, and their scattered values are shown in gray. The scattering ranges values for the model parameters reported in Tab.2 Furthermore, IMU biases and scale factors, atmospheric density (ρ), wind direction (λ), and mean wind speed (W), the latter shown in Fig. 5a (black line for the nominal value of mean wind and blue lines for its scattered values), are randomly specified within the ranges shown in Tab.3.

Table 2   Scattering ranges for the Monte Carlo campaign.

			LV model parameters			
δ_y	δ_z	C_a	C_{N_α}	C_{Y_β}	T	m
± 0.1 deg	± 0.1 deg	$\pm 10\%$	$\pm 10\%$	$\pm 10\%$	$\pm 2\%$	follows the mass-flow rate Eq.(96)

Table 3   Scattering ranges for the Monte Carlo campaign.

			IMU and atmospheric parameters			
$\lambda_a|_{t=0}$	$\lambda_\omega|_{t=0}$	$\beta_a|_{t=0}$	$\beta_\omega|_{t=0}$	W	λ	ρ
± 50 ppm	± 30 ppm	$\pm 100\,\mu$g	± 0.02 deg/h	$\pm 20\%$	± 180 deg	$\pm 5\%$
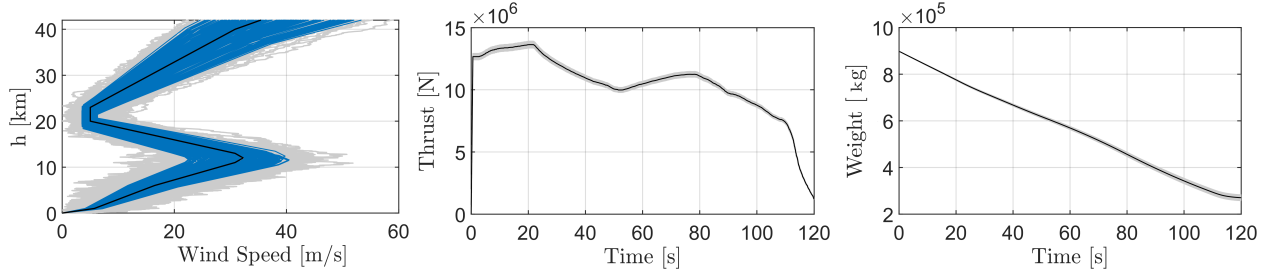
(a) Scattered values of mean wind intensity vs. altitude

(b) Scattered thrust vs. time

(c) Scattered mass vs. time

Fig. 5   Monte Carlo campaign: nominal values (black lines), scattered values (grey lines), scattered wind mean (blue lines).

Following filter tuning, the covariance matrix of measurement noise $\boldsymbol{R}$, assumed diagonal with dimension coherent with Eq.(80), reads

$$\boldsymbol{R} = \text{diag}\Big((9.81 \times 10^{-6})^2 \cdot \frac{\sigma_{a,y}^2}{T_s}, (9.81 \times 10^{-6})^2 \cdot \frac{\sigma_{a,z}^2}{T_s}, \sigma_{w_{v,x}}^2, \sigma_{w_{v,y}}^2, \sigma_{w_{v,z}}^2, \sigma_{w_T}^2, \left(\frac{\pi}{180}\right)^2 \cdot \sigma_{\sigma_\delta}^2,$$
$$, \sigma_{w_{r,w,x}}^2, \sigma_{w_{r,w,y}}^2, \sigma_{w_{r,w,z}}^2, 1.4^2, 1.4^2\Big) \tag{97}$$

with $T_s = 0.005$, that is, the IMU sample time. The majority of its nonzero elements correspond to the squares of the standard deviations of the noises in the measurement equations, with the σ values reported in Table1. The covariance matrix of process noise, $\boldsymbol{Q}$, is as follows

$$Q = \text{diag}\left((9.81 \times 10^{-6})^2 \cdot \sigma_{a,x}^2, \left(\frac{\pi}{180}\right)^2 \frac{1}{60} \cdot \sigma_{\omega,x}^2, \left(\frac{\pi}{180}\right)^2 \frac{1}{60} \cdot \sigma_{\omega,y}^2, \left(\frac{\pi}{180}\right)^2 \frac{1}{60} \cdot \sigma_{\omega,z}^2, \left(\frac{\pi}{180}\right)^2 \cdot \sigma_{\delta}^2, 7^2, 1^2\right.$$

$$1^2, 2.5^2, 0.6 \times 10^{-3}, 1.8 \times 10^{-3}, \left(\frac{\pi}{180}\right)^2 \frac{1}{60^3} \cdot \sigma_{wb_{\omega,x}}^2, \left(\frac{\pi}{180}\right)^2 \frac{1}{60^3} \cdot \sigma_{wb_{\omega,y}}^2, \left(\frac{\pi}{180}\right)^2 \frac{1}{60^3} \cdot \sigma_{wb_{\omega,z}}^2,$$

$$(9.81 \times 10^{-6})^2 \frac{1}{60} \cdot \sigma_{wb_{a,x}}^2, (9.81 \times 10^{-6})^2 \frac{1}{60} \cdot \sigma_{wb_{a,y}}^2, (9.81 \times 10^{-6})^2 \frac{1}{60} \cdot \sigma_{wb_{a,z}}^2,$$

$$\left. 0.1 \times 10^{-10}, 0.1 \times 10^{-10}, 0.1 \times 10^{-10}, 0.1 \times 10^{-6}, 0.1 \times 10^{-10}, 0.1 \times 10^{-10}\right) \tag{98}$$

where some unit conversion is needed to use the IMU data in Tab.1 which are associated with the power spectral density PSD of the IMU input signal. A Monte Carlo analysis of 200 simulation runs is conducted, with the same sampling frequency of 10 Hz for all sensors, in order to evaluate the consistency, robustness, and accuracy of the filter. Figure 6 shows the consistency of the airspeed velocity and wind components, whereas Fig. 7 shows the consistency of the attitude and position states. Figure 8 reports the consistency of the estimation of elastic rotations at the gimbal and scale factor on a_x. The continuous black lines represent the standard deviation of the estimation error as predicted by the filter, expressed as 3-σ values, while the dashed blue lines give the standard deviations of the errors calculated directly from the Monte Carlo samples, once again computed as 3-σ, the consistency of the filter being provided by the overlapping of these two lines. Finally, the continuos blue line corresponds to the mean of the samples.

The expected value of the error is very close to zero, which means that the filter works as an unbiased filter, in line with the theoretical expectations for the minimum mean square error (MMSE) estimators. It is noteworthy in Fig. 6 that the filter slightly underestimates the error covariance in the time range between 40 s and 60 s, while it overestimates the error covariance in the latter part of the flight (after 80 s). The former discrepancy may be attributed to the dynamic pressure reaching its peak, causing uncertain aerodynamic terms to exert more influence on the force balance than other factors. On the other hand, in the last part of the flight, wind turbulence diminishes significantly compared to level in the troposphere and, consequently, the constant value of process noise adopted in this study for the sake of simplicity proves to be inadequate to capture this effect. After approximately 80 s of flight the low value of density make the wind poorly observable, so that the covariance of the filter starts to increase. It is also apparent in Fig. 4c that the downward component of the wind is poorly estimated in the last part of the flight.
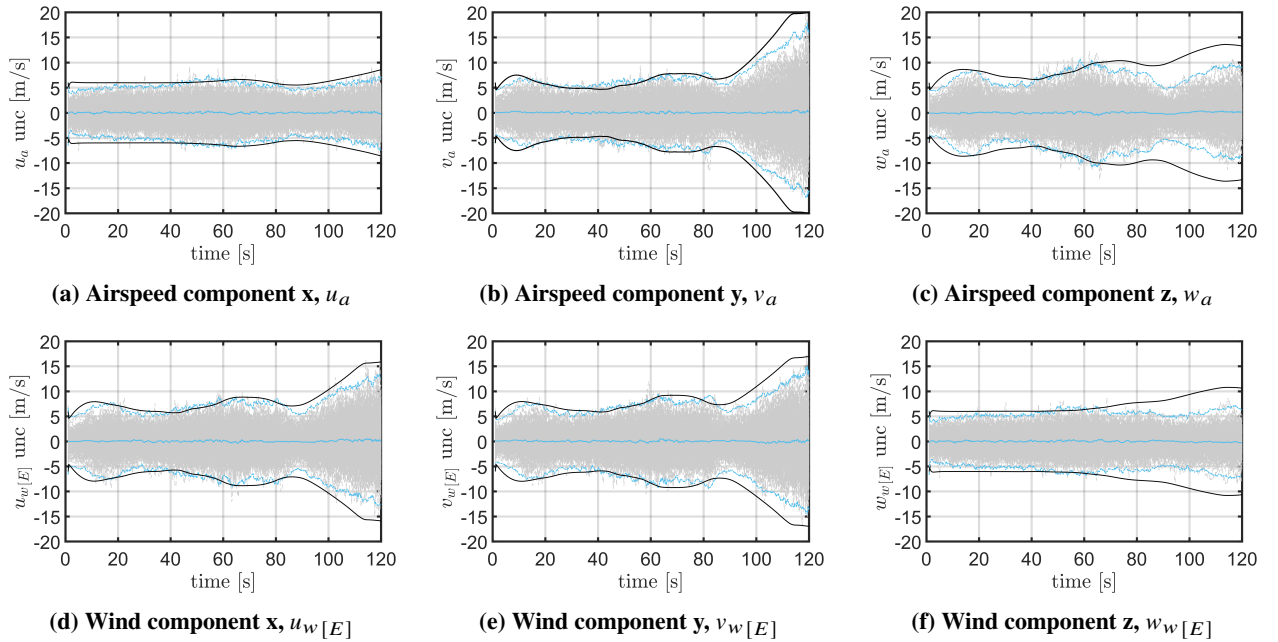

(a) **Airspeed component x, u_a**

(b) **Airspeed component y, v_a**

(c) **Airspeed component z, w_a**

(d) **Wind component x, $u_{w[E]}$**

(e) **Wind component y, $v_{w[E]}$**

(f) **Wind component z, $w_{w[E]}$**

Fig. 6   Monte Carlo campaign: CMEKF 3σ covariance (black lines), estimation errors (grey lines), mean of MC samples (continuous blue lines), covariance of MC samples (dotted blue lines).

The results on the evaluation of attitude and position, reported in Fig. 7, show that the filter exhibits a very

good consistency and convergence of the estimates. In particular, Fig. 7a shows that the bound of the samples is slightly underestimated between 80 s and 100 s, due to an inaccurate estimation of the bound of the scale factor $\lambda_{a,x}$ (reported in Fig.8c). The errors in the states associated with elastic displacements, as illustrated in Figure 8, indicate an overestimation of the filter's covariance compared to the covariance of the samples. However, they serve to enable the filter to incorporate the uncertainty associated with these states in estimating the other state variables. Particularly, this approach resulted in a more accurate estimate compared to including them as parameters in the consider filter. Finally, Fig.9 illustrates the uncertainty in the estimation of aerodynamic angles obtained a posteriori.
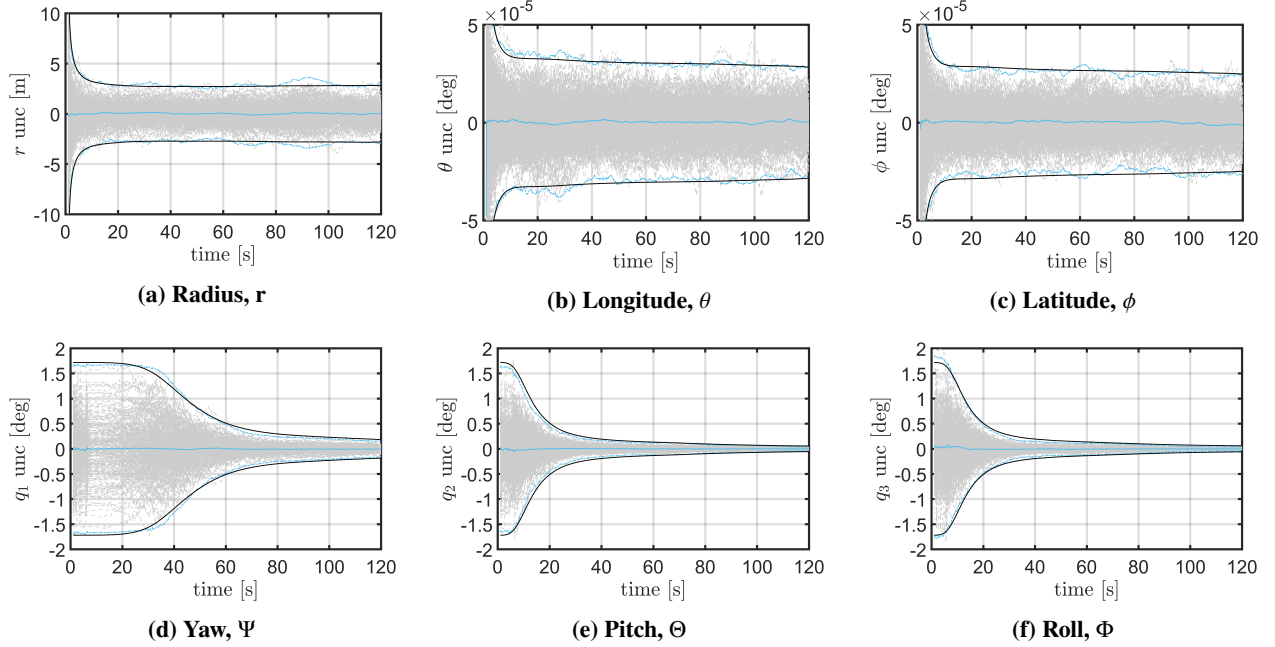

(a) Radius, r

(b) Longitude, θ

(c) Latitude, ϕ

(d) Yaw, Ψ

(e) Pitch, Θ

(f) Roll, Φ

Fig. 7 **Monte Carlo campaign: CEKF 3σ covariance (black lines), estimation errors (grey lines), mean of MC samples (continuous blue lines), covariance of MC samples (dotted blue lines).**
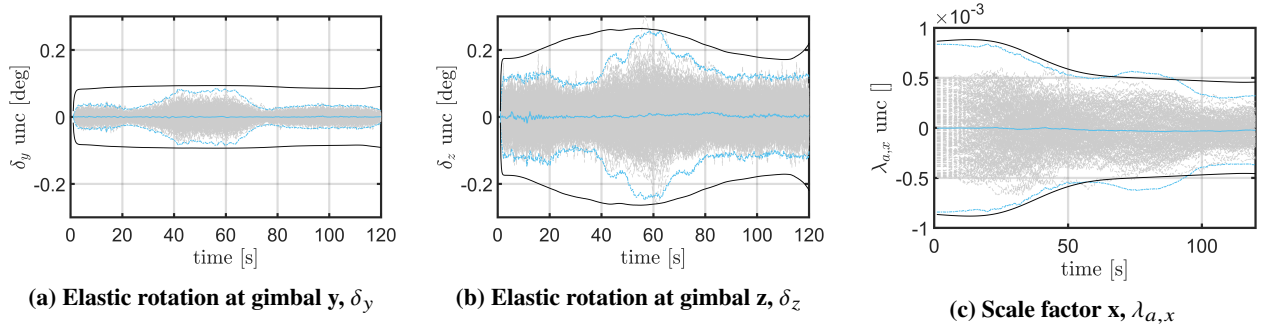

(a) Elastic rotation at gimbal y, δ_y

(b) Elastic rotation at gimbal z, δ_z

(c) Scale factor x, $\lambda_{a,x}$

Fig. 8 **Monte Carlo campaign: CEKF 3σ covariance (black lines), estimation errors (grey lines), mean of MC samples (continuous blue lines), covariance of MC samples (dotted blue lines).**

A better understanding of these trends can be obtained by examining the RMSE values reported in Tab. 4, where the filter performance is evaluated in terms of root-mean-square error (RMSE) on α, β, $\alpha_{\text{tot}} = \sqrt{\alpha^2 + \beta^2}$, airspeed components u_a, v_a, w_a and wind velocity components $u_{w[E]}, v_{w[E]}, w_{w[E]}$. The RMSE of the estimated values is computed as

$$x_{\text{RMSE}} = \sqrt{\frac{1}{t_f} \int_0^{t_f} x^2(t)dt} \tag{99}$$

(a) Angle of attack, α
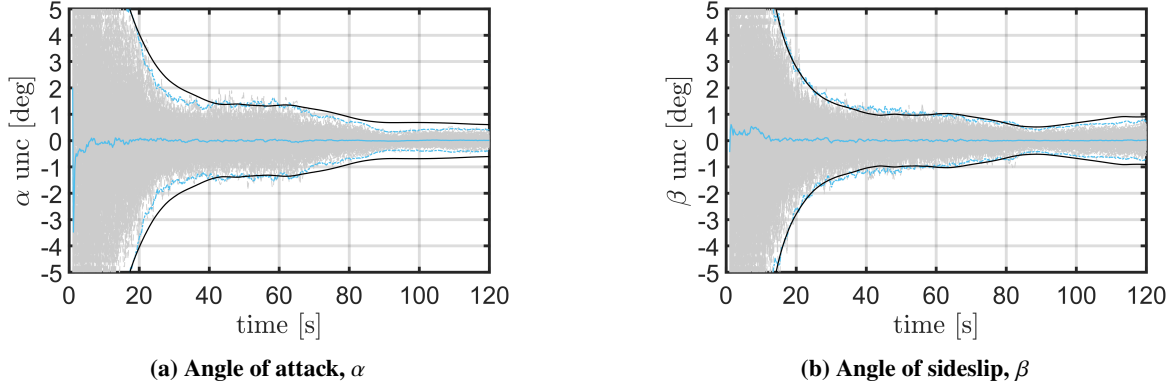
(b) Angle of sideslip, β

Fig. 9 Monte Carlo campaign: CEKF 3σ covariance (black lines), estimation errors (grey lines), mean of MC samples (continuous blue lines), covariance of MC samples (dotted blue lines).

where $x(t)$ stays for the variable of interest.

Table 4 RMSE on estimated variables (gravity turn phase).

				RMS error (t > 10 s)				
α [deg]	β [deg]	α_{tot} [deg]	u_a [m/s]	v_a [m/s]	w_a [m/s]	$u_{w[E]}$ [m/s]	$v_{w[E]}$ [m/s]	$w_{w[E]}$ [m/s]
0.51	0.82	0.96	2.09	2.27	2.68	2.90	2.14	2.10

In terms of the estimation of aerodynamic angles (α_{tot}), the results indicate adequate accuracy, with a maximum RMSE of approximately 0.96 degrees. It is worth observing that the estimation of the vertical wind component demonstrates a slightly higher accuracy compared to v_{w_N} and v_{w_E} because it consistently exhibits a lower RMSE, but this is probably due to the limited steady-state variation of the vertical wind component with altitude, in contrast to the other two components that show altitude-dependent variations. Note that the evaluation of the RMSE does not include the initial 10 seconds of simulation (from lift-off to the end of pitch-over) because of the uneven and large variations of the aerodynamic angles associated with the low speed of the vehicle. Table 5 reports the RMSE values of both position

Table 5 RMSE on estimated variables (gravity turn phase).

			RMS error on position and attitude (t > 10 s)		
Ψ [deg]	Θ [deg]	Φ [deg]	r [m]	θ [deg]	ϕ [deg]
0.228	0.176	0.124	0.770	1.331×10^{-5}	7.755×10^{-6}

and attitude errors. In contrast to the initial attitude uncertainty with a 1-σ value of 0.57 deg, a significant reduction in attitude error has been obtained with the filtering process, indeed during the gravity turn phase, measured in terms of Root Mean Square Error (RMSE) there is a reduction of 60%, 70%, and 80% for yaw, pitch, and roll, respectively. Additionally, the positional range error is maintained at precision levels below 1 m as result of the filtering process. Considering that the Global Navigation Satellite System (GNSS) measurement has a precision of approximately 6 m for each component, this improvement in position accuracy represents a tenfold enhancement. In the end, measurement residuals are shown in Fig.10. Grey lines represent the residual errors in measurement estimations Δy_k, while the red curves represent the RMS over the Monte Carlo simulations per each time of $\pm 3\sqrt{\text{diag}(S)}$, where diag($S$) indicates the diagonal elements of the measurement residual covariance matrix S. It is apparent that each vector of residuals is contained within the bounds imposed by the measurement residual covariance matrix.

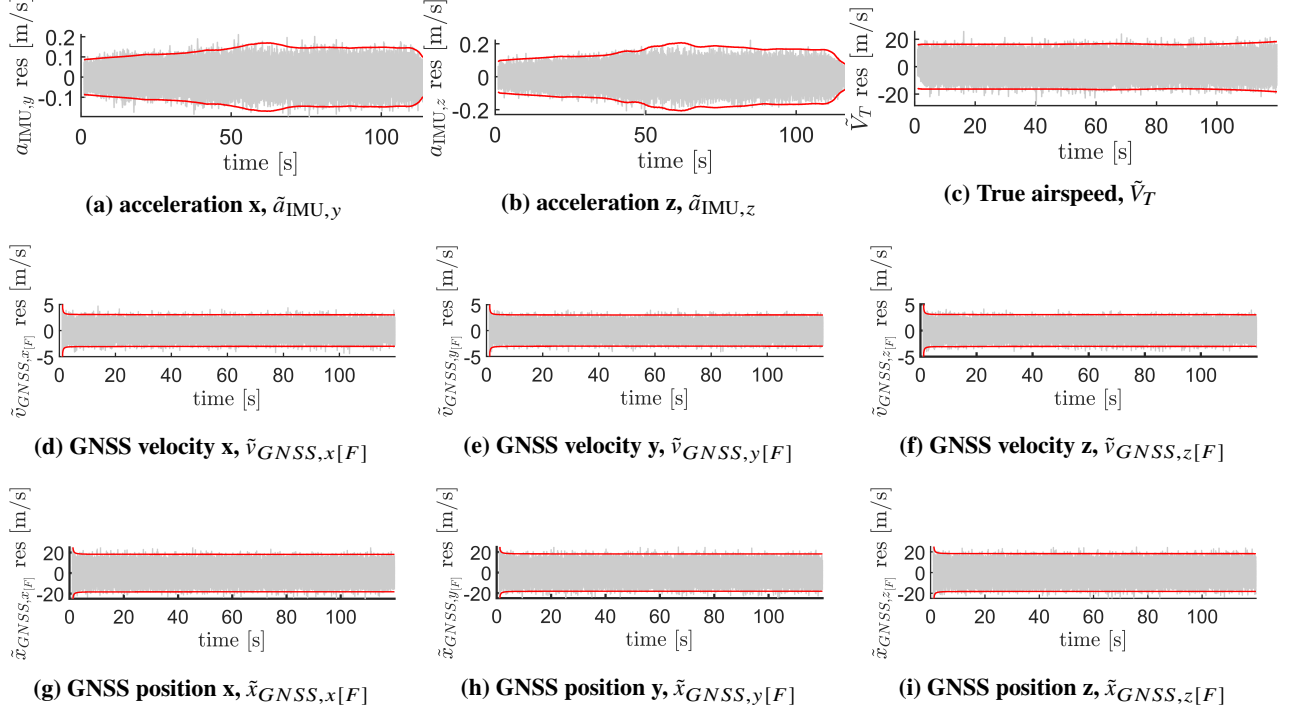**Fig. 10 Monte Carlo campaign: CEKF 3σ measurement residual covariance covariance (red lines), measurement residuals (grey lines).**

V. Conclusion

A filtering technique based on a Consider Multiplicative Extended Kalman filter (CMEKF) has been presented with the aim of estimating the aerodynamic angles and the atmospheric wind components during the ascent flight of a large, flexible, launch vehicle (LV). The filter presents a novel formulation where the airspeed components are considered as state variables in place of the aerodynamic angles. A multiplicative error quaternion formulation for attitude estimation is adopted to improve the accuracy over traditional (additive) formulation. The preliminary analysis here presented takes into consideration four significant sources of uncertainty, that are often neglected in similar works, that is i) the deviation of thrust direction due to elastic effects at the gimbal location, ii) the influence of non-collocated IMU and GNSS sensors, iii) the presence of systematic errors, such as bias, non-orthogonality, and scale factors, and iv) large discrepancies between pre-flight forecast and in-flight values of the magnitude and direction of the wind.

The obtained results suggest the suitability and effectiveness of the filter in a simulation scenario with high-turbulence wind and scattered (yet close-to-nominal) flight conditions. A Monte Carlo analysis has been carried out, scattering a considerable amount of structural, aero-propulsive, and flight parameters, to comprehensively assess their impact on the filter performance. In this respect, the obtained results are encouraging as the novel filter formulation provides a suitable tool to estimate LV aerodynamic angles and wind components by using a small subset of commonly used pre-flight data and in-flight measurements.

Future research endeavors could explore the estimation of atmospheric characteristics as a distinct aspect, rather than incorporating them as uncertainties within the system alongside a correction of aero-propulsive coefficients that characterize the LV. Enhancement in estimation accuracy can be achieved by employing a smoothing technique, to avoid the intrinsic limitations of sequential filtering methods. Smoothing techniques such as the Rauch–Tung–Striebel (RTS) or Fraser Potter smoother are deemed of particular interest and promise avenues for improvement in the overall estimation process. Additionally, real flight data could be used to further validate and refine the filter's performance. This work has implications for enhancing the safety, reliability, and efficiency of launch vehicle operations, contributing to the advancement of aerospace technology and exploration.

Appendix

A. Reference frames

1. Earth-centered inertial (ECI)

The not-rotating ECI frame, $\mathcal{F}_I$, has the z-axis normal to the equatorial plane, coinciding with the Earth rotation axis and pointing to the North Pole. The x-axis lies in the equatorial plane pointing towards the vernal equinox. The y-axis is in the equatorial plane and completes the right-handed Cartesian system.

2. Earth-centered Earth-fixed (ECEF)

The rotating ECEF reference frame, $\mathcal{F}_F$, has the z-axis defined as for the ECI frame. The x-axis lies in the equatorial plane pointing towards the Greenwich meridian, and the y-axis is in the equatorial plane.

3. North-East-Down (NED)

The NED frame, $\mathcal{F}_E$, has the origin located at the vehicle center of gravity (c.g.), and is oriented with the x-axis pointing in the direction of North Pole, The z-axis is perpendicular to the x-axis and oriented along the local vertical, and the y-axis completes the right-hand frame.

4. Body-fixed (B)

The B frame, $\mathcal{F}_B$, is fixed to the principal axes of inertia of the vehicle, assumed rigid, with origin in the c.g. The x-axis is along the vehicle longitudinal axis, the y-axis is arbitrarily chosen in the plane orthogonal to the x-axis, due to the axial symmetry of the LV model, while the z-axis completes the right-handed frame.

5. Nozzle-fixed (N)

The N frame, $\mathcal{F}_N$, is fixed to the nozzle with origin in its c.g. The x-axis points along the nozzle pivot point, the y-axis is perpendicular to the axis of symmetry of the nozzle and is parallel to the y-axis of the frame $\mathcal{F}_B$, pointing to the same direction, while the z-axis completes the right-handed frame.

6. Structural-fixed (S)

The S frame has its origin on the top of the nose of the LV with x-axis direct to the c.g. and the y-axis aligned with the y-axis in $\mathcal{F}_B$, the z-axis completes the right-handed frame.

B. Force equation

The momentum equation for the LV is written as

$$m[\dot{v} + (\omega_{BI} + \mathcal{R}_{BF}\omega_\oplus) \times v] + \mathcal{R}_{BF}[\omega_\oplus \times (\omega_\oplus \times \mathbf{p}_{[F]})] = \mathbf{F} \tag{100}$$

where $\mathbf{F} = \mathbf{F}_A + \mathbf{F}_g + \mathbf{T}$, $v = \mathbf{V}_a + v_w$, and the wind velocity vector in $\mathcal{F}_B$ is expressed as

$$v_w = \mathcal{R}_{BE} \begin{bmatrix} v_{w_N} \\ v_{w_E} \\ v_{w_D} \end{bmatrix} \tag{101}$$

Equation (100) is rewritten in terms of non gravitational acceleration at c.g. location ($\mathbf{a}$) as

$$\dot{v} = \mathbf{a} - (\omega_{BI} + \mathcal{R}_{BF}\omega_\oplus) \times v - \mathcal{R}_{BF}[\omega_\oplus \times (\omega_\oplus \times \mathbf{p}_{[F]})] \tag{102}$$

By expressing $\dot{v}$ in term of wind velocity, Eq. (102) reads

$$\dot{\mathbf{V}}_a = -\dot{v}_w + \mathbf{a} - (\omega_{BI} + \mathcal{R}_{BF}\omega_\oplus) \times \mathbf{V}_a - (\omega_{BI} + \mathcal{R}_{BF}\omega_\oplus) \times v_w + \varpi + f_g \tag{103}$$

where $\varpi = -\mathcal{R}_{BF}[\omega_\oplus \times (\omega_\oplus \times \mathbf{p}_{[F]})]$ and f_g the gravity force.

Acknowledgements

References

[1] Karlgaard, C. D., Kutty, P., O'Farrell, C., Blood, E., Ginn, J., and Schoenenberger, M., "Reconstruction of Atmosphere, Trajectory, and Aerodynamics for the Low-Density Supersonic Decelerator Project," *Journal of Spacecraft and Rockets*, Vol. 56, No. 1, 2019, pp. 221–240.

[2] Vitale, A., Corraro, F., Bernard, M., and De Matteis, G., "Unscented Kalman Filtering for Reentry Vehicle Identification in the Transonic Regime," *Journal of Aircraft - J AIRCRAFT*, Vol. 46, 2009, pp. 1649–1659. https://doi.org/10.2514/1.42256.

[3] Dutta, S., and Braun, R. D., "Statistical entry, descent, and landing performance reconstruction of the mars science laboratory," *Journal of Spacecraft and Rockets*, Vol. 51, No. 4, 2014, pp. 1048–1061.

[4] Boelitz, F., Gatt, P., and Martin, A., *Launch Vehicle Wind Look Ahead Guidance for Ascent Load Management*, ???? https://doi.org/10.2514/6.2003-5499, URL https://arc.aiaa.org/doi/abs/10.2514/6.2003-5499.

[5] Oh, G., Park, J., Park, J., Lee, H., Kim, Y., Shin, S.-J., Ahn, J., and Cho, S., "Load relief control of launch vehicle using aerodynamic angle estimation," *Proceedings of the Institution of Mechanical Engineers, Part G: Journal of Aerospace Engineering*, Vol. 232, No. 8, 2018, pp. 1598–1605. https://doi.org/10.1177/0954410017699435, URL https://doi.org/10.1177/0954410017699435.

[6] Simplício, P., Marcos, A., and Bennani, S., "New control functionalities for launcher load relief in ascent and descent flight," *Proceedings of the 8th European Conference for Aeronautics and Aerospace Sciences*, 2019. https://doi.org/10.13009/EUCASS2019-275.

[7] Simplício, P., Marcos, A., and Bennani, S., "Launcher flight control design using robust wind disturbance observation," *Acta Astronautica*, Vol. 186, 2021, pp. 303–318. https://doi.org/https://doi.org/10.1016/j.actaastro.2021.05.044.

[8] Crassidis, J. L., and Junkins, J. L., *Optimal estimation of dynamic systems*, Vol. 2, Chapman & Hall/CRC Boca Raton, FL, 2004.

[9] D'Antuono, V., Di Monaco, G., Zavoli, A., De Matteis, G., Pizzurro, S., and Cavallini, E., "Estimation of Aerodynamic angles and Wind Components for a Launch Vehicle," *AAS/AIAA Astrodynamics Specialist Conference at Charlotte, NC, United States*, 2022.

[10] Shuster, M. D., "Survey of attitude representations," *Journal of the Astronautical Sciences*, Vol. 41, No. 4, 1993, pp. 439–517.

[11] Du, W., "Dynamic modeling and ascent flight control of Ares-I Crew Launch Vehicle," Ph.D. thesis, Iowa State University, Digital Repository, Iowa State University, 2010. https://doi.org/https://doi.org/10.31274/etd-180810-1029.

[12] Barrows, T. M., and Orr, J. S., *Dynamics and Simulation of Flexible Rockets*, Academic Press, 2020.

[13] Vandersteen, J., Bennani, S., and Roux, C., "Robust Rocket Navigation with Sensor Uncertainties: VEGA Launcher Application," *Journal of Spacecraft and Rockets*, Vol. 55, No. 1, 2018, pp. 153–166. https://doi.org/10.2514/1.a33884.

[14] Karlgaard, C. D., Beck, R. E., Derry, S. D., Brandon, J. M., Starr, B. R., Tartabini, P. V., and Olds, A. D., "Ares-I-X Trajectory Reconstruction: Methodology and Results," *Journal of Spacecraft and Rockets*, Vol. 50, No. 3, 2013, pp. 641–661.

[15] Di Monaco, G., D'Antuono, V., Zavoli, A., De Matteis, G., Pizzurro, S., Cavallini, E., et al., "Trajectory Reconstruction of Launch Vehicle in Atmospheric Flight using the Unscented Kalman Filter," *AIAA Science and Technology Forum and Exposition, AIAA SciTech Forum 2023*, 2023.

[16] Vitale, A., Corraro, F., Bernard, M., and De Matteis, G., "Unscented Kalman filtering for reentry vehicle identification in the transonic regime," *Journal of aircraft*, Vol. 46, No. 5, 2009, pp. 1649–1659.

[17] Zanetti, R., and D'Souza, C., "Recursive implementations of the Schmidt-Kalman 'consider' filter," *The Journal of the Astronautical Sciences*, Vol. 60, No. 3-4, 2013, pp. 672–685.

[18] Lefferts, E. J., Markley, F. L., and Shuster, M. D., "Kalman filtering for spacecraft attitude estimation," *Journal of Guidance, control, and Dynamics*, Vol. 5, No. 5, 1982, pp. 417–429.

[19] Zanetti, R., and DeMars, K. J., "Joseph formulation of unscented and quadrature filters with application to consider states," *Journal of Guidance, Control, and Dynamics*, Vol. 36, No. 6, 2013, pp. 1860–1864.

[20] Zanetti, R., and DSouza, C., "Recursive implementations of the consider filter," Tech. rep., 2012.

[21] Johnson, D., "Terrestrial environment (climatic) criteria guidelines for use in aerospace vehicle development. 2008 revision," NASA/TM 2008-215633, 2008.